SANDIA REPORT
SAND2006-7265
Unlimited Release
Printed November 2006

LDRD Final Report on Using Chaos for Ultrasensitive Coherent Signal Detection

Sebastian Wieczorek, Weng Chow, Geoffrey Torrington

Prepared by
Sandia National Laboratories
Albuquerque, New Mexico 87185 and Livermore, California 94550

Sandia is a multiprogram laboratory operated by Sandia Corporation,
a Lockheed Martin Company, for the United States Department of Energy's
National Nuclear Security Administration under Contract DE-AC04-94AL85000.

Issued by Sandia National Laboratories, operated for the United States Department of Energy by Sandia Corporation.

Available to DOE and DOE contractors from
U.S. Department of Energy
Office of Scientific and Technical Information
P.O. Box 62
Oak Ridge, TN 37831

Telephone: (865) 576-8401
Facsimile: (865) 576-5728
E-Mail: reports@adonis.osti.gov
Online ordering: http://www.osti.gov/bridge

Available to the public from
U.S. Department of Commerce
National Technical Information Service
5285 Port Royal Rd.
Springfield, VA 22161

Telephone: (800) 553-6847
Facsimile: (703) 605-6900
E-Mail: orders@ntis.fedworld.gov
Online order: http://www.ntis.gov/help/ordermethods.asp?loc=7-4-0#online

SAND 2006-7265
Unlimited Release
Printed November 2006

LDRD Final Report on Using Chaos for Ultrasensitive Coherent Signal Detection

Sebastian Wieczorek, Weng Chow
Semiconductor Materials and Device Sciences Department

and

Geoffrey Torrington
Sensor Subsystems Department

Sandia National Laboratories
P. O. Box 5800
Albuquerque, NM 87185-1086

Abstract

A quantum optical approach is proposed and analyzed as a solution to the problem of detecting weak coherent radiation in the presence of a strong incoherent background. The approach is based on the extreme sensitivity of laser dynamical nonlinearities to the coherence of external perturbation. This sensitivity leads to dynamical phase transitions that may be employed for detecting the presence of external coherent radiation. Of particular interest are the transitions between stable and chaotic states of laser operation. Using a baseline scheme consisting of a detector laser operating with a Fabry-Perot cavity, we demonstrated significant qualitative and quantitative differences in the response of the detector laser to the intensity and coherence of the external signal. Bifurcation analysis revealed that considerable modification to the extension of chaotic regions is possible by tailoring active medium and optical resonator configurations. Our calculations showed that with semiconductor lasers, destabilization can occur with a coherent external signal intensity that is over six orders of magnitude smaller than the detector laser's intracavity intensity. Discrimination between coherent and incoherent external signal also looks promising because of the over four orders of magnitude difference in intensity required for inducing chaos-like behavior. These results suggest that the proposed approach may be useful in laser sensor applications, such as satellite Laser Threat Warning Receivers (LTWR).

Table of Contents

I. Introduction

The underlying challenge of developing laser sensors, for applications such as satellite laser threat warning receivers (LTWR), is the requirement to detect a weak coherent signal in the presence of a strong incoherent background. Present attempts to discriminate between signal and noise involve classical approaches using spatial or temporal coherence. Demanding mission requirements make the engineering of these passive detection systems very difficult. Largely unexplored are quantum optical solutions.

In this LDRD project, we proposed and analyzed a quantum optical approach based on the extreme sensitivity of laser dynamical nonlinearities to external perturbation coherence. The approach uses an experimental setup that is very similar to heterodyne detection. An important difference is that the mixing of the signal and reference beams occurs *inside* instead of outside the local oscillator (see Fig. 1). With intracavity mixing, we change entirely the character of the detection mechanism. Owing to the dynamical nonlinearities arising from the coupling between optical resonator and active medium, the possibility exists that a very low intensity ($<10^{-6}$ of intracavity intensity) and detuned coherent light injection can induce a laser to cross bifurcation boundaries separating stable from chaotic operation, whereas even a much stronger incoherent injected signal is unable to do so.

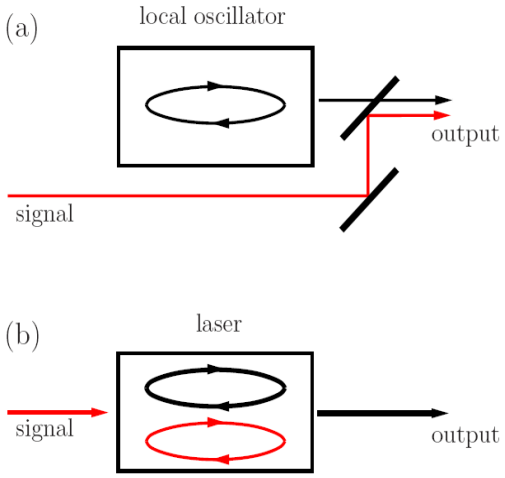

Fig. 1. Sketch of (a) heterodyne detection setup and (b) proposed scheme based on stable to chaos dynamical transition.

The primary goal of this one-year study was to understand the physics sufficiently well to determine the viability of our scheme for LTWR applications. Among the many questions that should be answered, the most important is the detectable signal strength and achievable detection bandwidth. For engineering implementation, one needs to also consider the controllability of the bifurcation conditions, and the practicality of engineering the detector laser.

To address the above questions, we first review past research relevant to our problem (Sec. II). Section III describes the theoretical model used in the investigation. With this model, we performed global mapping calculations that identify regions of steady state or continuous-wave (cw), oscillatory, and chaotic operation. Bifurcation maps for the noiseless case are presented in Sec. IV, together with a discussion of the details of the transitions between dynamical regions for different experimental conditions. Section V describes the effect of noise in the external signal or detector laser.

II. Review of external-signal-induced laser dynamics

Nonlinear dynamics of laser systems is a very active research field. For the last two decades, the focus has been on understanding instabilities in the widely-used semiconductor lasers. A typical free-running semiconductor laser is a dynamically stable system, capable only of damped periodic oscillation (relaxation oscillation). However, this can change drastically when the laser is coupled to another laser or subjected to a stimulus, such as optical injection or external optical feedback. In these cases, semiconductor lasers have been shown to undergo a number of bifurcations, leading to periodic, quasiperiodic, and chaotic oscillations.

Much effort has been devoted to researching the bifurcations and ensuing complicated dynamics in semiconductor lasers with external perturbations[1-3]. It is well established that the laser response to an external optical signal strongly depends on the linewidth-enhancement factor α [4-8], which quantifies the extent the carrier-induced refractive index change affects the laser linewidth and lateral mode structure. However, other aspects of externally perturbed laser dynamics are less well understood. For example, some studies suggested that quantities such as the photon and carrier decay rates, differential gain and mode confinement factor have less influence on semiconductor-laser dynamics than α[6-7], while others reported strong dependence of coupled-semiconductor-laser dynamics on the ratio of carrier and cavity decay rates[8]. Furthermore, while there are reports on the influence of fluctuations (incoherence) in the external optical field on laser instabilities[9], a more in-depth understanding is necessary for us to make a decision on the applicability of our LTWR scheme.

III. Rate equation model

The detector laser is treated semiclassically, i.e., with Maxwell's equation describing the intracavity laser field and Schrodinger equation describing the gain medium. Additionally, it is assumed that relaxation rates are such that the active-medium polarization adiabatically follows the variations in the intracavity electric field and population inversion, with the carrier population described by quasiequilibrium distributions. Under these conditions, the complex intracavity-field amplitude, E and the population density, N evolve in time according to,

$$\frac{dE}{dt} = i\,2\pi\Delta\,E + \frac{c}{n_b}\Gamma\xi(N - N_{th})(1 - i\alpha)E + F_E(t) + \frac{c\sqrt{T}}{2n_bL}|E_i|e^{-i\phi_i(t)}$$

$$\frac{dN}{dt} = \Lambda - \gamma_N N - \frac{\epsilon_0 n_b c}{\hbar\nu}\left[g_{th} + \xi(N - N_{th})\right]|E|^2.$$

In the above equations, the effects of external signal are taken into account by the terms containing the external signal amplitude E_i. Also, the phase of E is referenced to that of external signal, Δ is the detuning between injected and free-running laser central frequencies, Γ is the confinement factor, ξ is the differential gain at threshold carrier density, α is the linewidth enhancement factor, Λ is the pump rate, γ_E and γ_N are the photon and population decay rates, respectively, c is the speed of light in vacuum and n_b is the background refractive index. The threshold carrier density and local gain in the free-running detector laser are given by

$$N_{th} = N_{tr} + \frac{n_b \gamma_E}{2c\Gamma\xi},$$
$$g_{th} = \frac{n_b \gamma_E}{2c\Gamma},$$

where N_{tr} is the transparency carrier density. The effects of noise are represented by the Gaussian random variable,

$$F_E(t) = F'_E(t) + iF''_E(t)$$

with

$$\langle F'_E(t)\rangle = \langle F''_E(t)\rangle = 0,$$
$$\langle F'_E(t)F''_E(t')\rangle = 0,$$
$$\langle F'_E(t)F'_E(t')\rangle = \langle F''_E(t)F''_E(t')\rangle = \frac{\hbar\nu}{\epsilon_0\epsilon_b} C_{sp}\gamma_N N\delta(t-t')$$

where ν is the lasing frequency, C_{sp} is the fraction of spontaneous emission contributing to the lasing mode. To describe phase noise in the external signal, we allow for a fluctuating external signal phase $\varphi_i(t)$ with time derivative

$$\frac{d\phi_i}{dt} = F_\phi(t)$$

where

$$\langle F_\phi(t)\rangle = 0,$$
$$\langle F_\phi(t)F_\phi(t')\rangle = 2D_\phi\delta(t-t')$$

With the above description, the resulting power spectrum of the external signal is a Lorentzian with a full width at half maximum of D_φ/π.

Table 1. Parameters for Lasers A and B used in the investigation

Parameter	Laser A	Laser B
N_{tr} (m^{-3})	2×10^{24}	2×10^{24}
ξ (m^2)	10^{-19}	10^{-19}
n_b	3.4	3.4
α	4	4
Γ	0.05	0.05
γ_N (s^{-1})	10^9	2×10^9
γ_{cav} (s^{-1})	10^{12}	10^{11}
λ (μm)	1	1
L (m)	10^{-6}	2×10^{-4}
T	0.01	0.2
C_{sp}	10^{-5}	10^{-5}

IV. Detection dynamics (noiseless case)

In this section, we describe the influence of the external signal on detector laser dynamics for two distinct detector laser configurations. In order to first understand intrinsic behavior, we neglect the noise contributions by setting $C_{sp} = D_{\varphi} = 0$. The results are summarized in bifurcation diagrams, presented for the two-dimensional plane of external signal intensity and detuning between external signal and detector laser frequencies. When either the external intensity or detuning is varied, qualitative changes in the lasing solutions indicate bifurcations. In the bifurcation diagrams, bifurcations curves divide the two-dimensional plane into regions of distinctly different dynamical behaviors and provide information on the sensitivity of the detector laser to signal intensity and detuning.

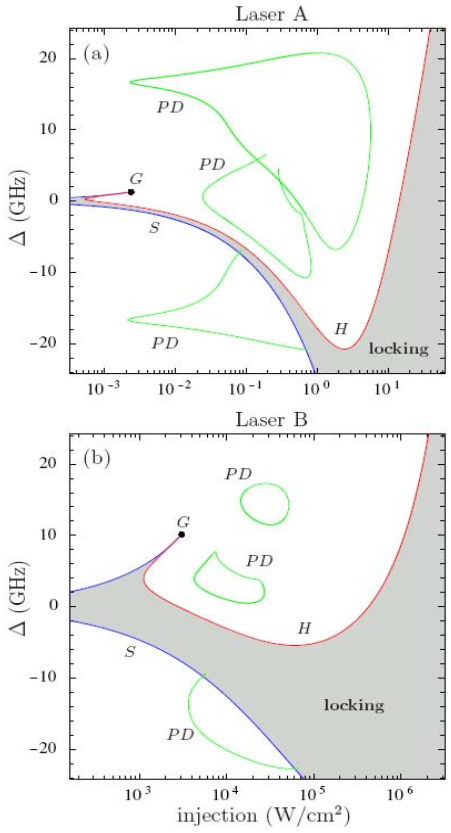

Fig. 2. Bifurcation diagrams for Lasers A and B operating at twice threshold and in the presence of coherent external signal.

A. Effects of active medium and optical resonator

Table 1 lists the values for the parameters characterizing Lasers A and B. The values are chosen so that between the two lasers, there is a factor of 2 difference in population decay rates and a factor of 10 difference in cavity decay rate. Figure 2 shows the bifurcation diagrams with both lasers operating at twice above threshold. A stable fixed point in the solutions of the system equations corresponds to phase locking of the

laser field to the external signal. One stable fixed point exists in the shaded region bounded by the saddle-node S and Hopf H bifurcation curves, which become tangent at the saddle-node-Hopf point G. Outside the shaded region one finds interesting solutions corresponding to periodic orbits of various periods, quasiperiodic tori, and chaotic attractors, all of which describe oscillating detector laser intensity. These intensity oscillations are periodic with frequency Δ near-zero signal intensity. With increasing signal intensity, a number of instabilities and complicated nonlinear dynamics appear before locking is reached at either the Hopf bifurcation H or saddle-node bifurcation S. Detailed bifurcation structures leading to complicated dynamics and chaos are discussed elsewhere[3]. In Fig. 2, only the period-doubling (PD) bifurcation curves are plotted. They indicate a typical instability involving periodic orbit of basic period and provide identification of regions of complicated dynamics in the system.

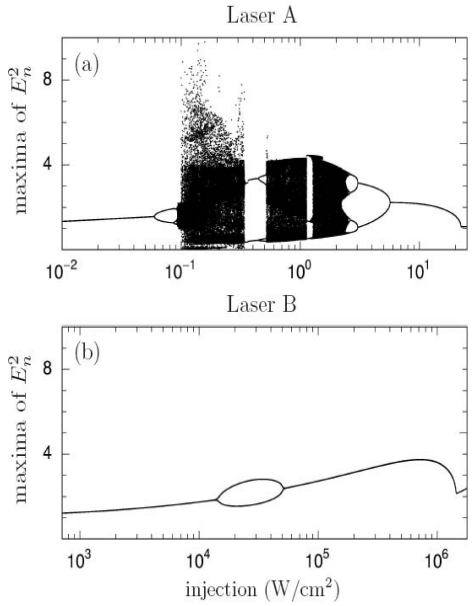

Fig. 3. Bifurcation transition shown as maxima of normalized laser intensity versus external signal intensity for (a) Laser A with Δ = 10 GHz and (b) Laser B with Δ = 15 GHz. Λ/Λ_{th} =2 for both lasers.

Figures 2(a) and 2(b) indicate that externally induced instabilities occur at roughly the same detuning values in the two lasers. However, in terms of the external-signal intensity, there are two aspects involving significant differences. One aspect is the striking quantitative difference in the external-signal intensity required to trigger laser instabilities and to achieve locking. Instabilities in laser A are triggered by an external-signal intensity that is almost 10^6 times lower than that required in laser B. Also, laser A requires less external-signal intensity to achieve locking over a wide range of detuning. The second aspect is the difference in the type of the dynamics induced by the external signal. Regions of complicated dynamics are appreciably smaller for laser B. Furthermore, laser B appears to have very few instabilities and no chaotic dynamics. In contrast, laser A undergoes a number of instabilities and shows a rich display of complicated and chaotic oscillations. This is illustrated in Fig. 3, where we plot the maxima of the oscillating laser intensity versus external-signal intensity for a fixed

detuning. Note that periodic orbit of a basic period has one maximum and periodic orbit of twice the basic period born in the period-doubling bifurcation has two maxima. Period-doubling bifurcation is indicated in Fig. 3 by the splitting of the single-maximum curve. Subsequent splitting, found in laser A, corresponds to subsequent steps in the period-doubling cascade leading to regions of complicated and chaotic oscillations, with windows of periodic dynamics. Clearly, laser A exhibits more complicated dynamics and stronger intensity oscillations than laser B, even in the presence of almost six orders of magnitude smaller external-signal intensity

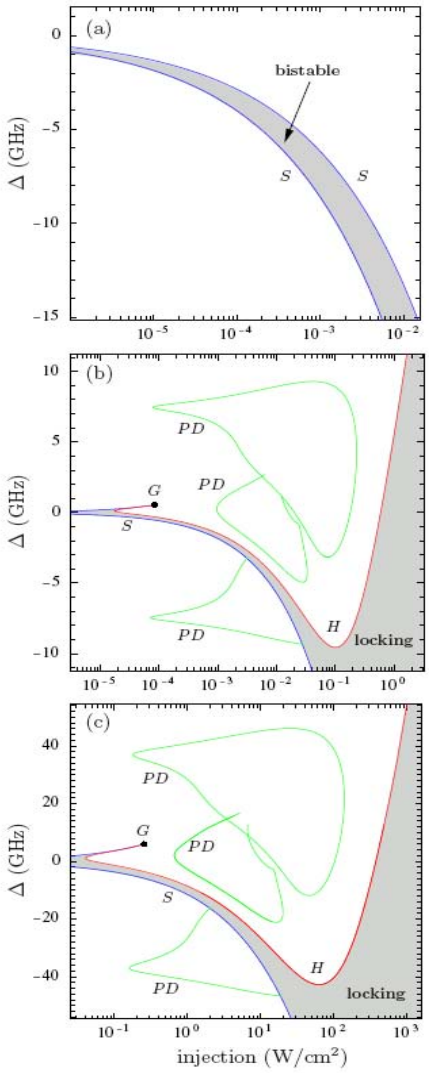

Fig. 4. Bifurcation diagram for Laser A with coherent external signal and excitation, Λ/Λ_{th} = (a) 1.0, (b) 1.2 and (c) 6.0

B. Effects of pump current

At twice the lasing threshold, the intracavity field intensities in lasers A and B are 41 kW/cm^2 and 560 kW/cm², respectively. In the case of laser A (B), this is approximately

10^7 (10^2) times more than the external-signal intensity required to trigger period-doubling bifurcation. In terms of maximizing detector sensitivity, Laser A is obviously the stronger candidate. Hence, we focus on its performance in this subsection, where the effects of changing the pump rate is investigated.

Figure 4 plots the bifurcation diagrams of Laser A operating just below threshold and at 1.2 and 6 times above threshold. At just below the lasing threshold [Fig. 4 (a)], the detector laser behaves as a bistable optical amplifier. In the Δ-I_{ext} plane, the bistable region is bounded by two saddle-node bifurcation curves S. As the pump rate is increased to slightly above the lasing threshold, a number of qualitative changes takes place, resulting in a completely different bifurcation diagram [Fig. 4 (b)], that is characteristic of a semiconductor laser. The original bistable region is replaced by a locking region and bifurcation curves involving Hopf (H) bifurcation, period-doubling (PD) bifurcations. Details of the transition between Figs. 4 (a) and 4 (b) are very interesting from a bifurcation theory aspect and their physical relevance is discussed in Section V, in relation to the case of system dynamics in the presence of noise. Figure 4 (c) shows that when pump current is further increased, to as much as six times above threshold, no qualitative changes take place, but there are significant quantitative changes. Specifically, there is an increase in the detuning range where instabilities and chaos can occur, together with an increase in the external-signal intensity required for triggering instabilities and chaos. Figures 4 (b) and 4 (c) clearly indicate a tradeoff between sensitivity and bandwidth.

V. Detection dynamics (noisy case)

A. Sensitivity to background noise

This section describes the effects of fluctuation in the detector laser by setting the noise parameters, $C_{sp} = 10^{-5}$ and $D_\varphi = 0$. A two-dimensional bifurcation analysis of the ordinary differential equations presented in Section III cannot be applied straightforwardly to the resulting stochastic differential equations. Instead, we have to focus on particular bifurcation transitions at fixed Δ and examine the power spectrum of the complex laser field amplitude E. Note that there exist various approaches to qualify nonlinear dynamics of noisy semiconductor lasers, and they include computations of time traces, Lyapunov exponents [7] and power spectrum. Our choice of the optical power spectrum is dictated by the fact that it provides a readily and widely used technique for qualifying dynamical output and instabilities in semiconductor laser experiments[10-13].

Substantial sensitivity to the noise terms may already be seen in the power spectra of the free-running lasers, where there is a large central peak surrounded by smaller side peaks. The former is the lasing mode and the latter are from relaxation oscillation and its higher harmonics. Figures. 5 - 7 depict the transition through a region of complicated and chaotic dynamics in the optically injected Laser A for Λ/Λ_{th} = 1.2, 2, and 6. For comparison, we show in the left column of each figure the power spectra in the absence of noise.

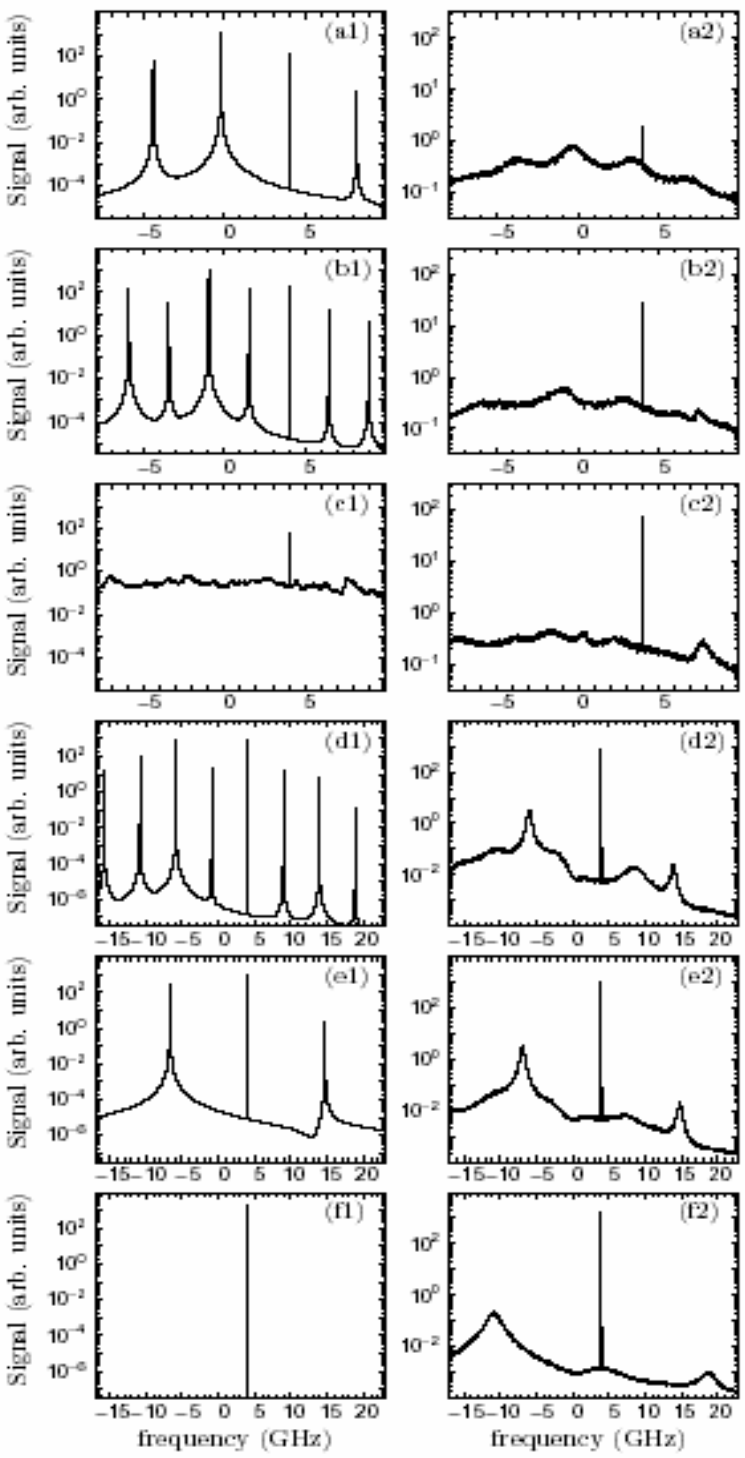

Fig. 5. Spectra for Laser A for noiseless (left column) and noisy (right column) cases. External signal intensities are (from top to bottom), 156 μW/cm^2, 3, 10, 181, 300 mW/cm^2 and 1W/cm^2. Also, $\Lambda/\Lambda_{th} = 1.2$ and $\Delta = 4$ GHz.

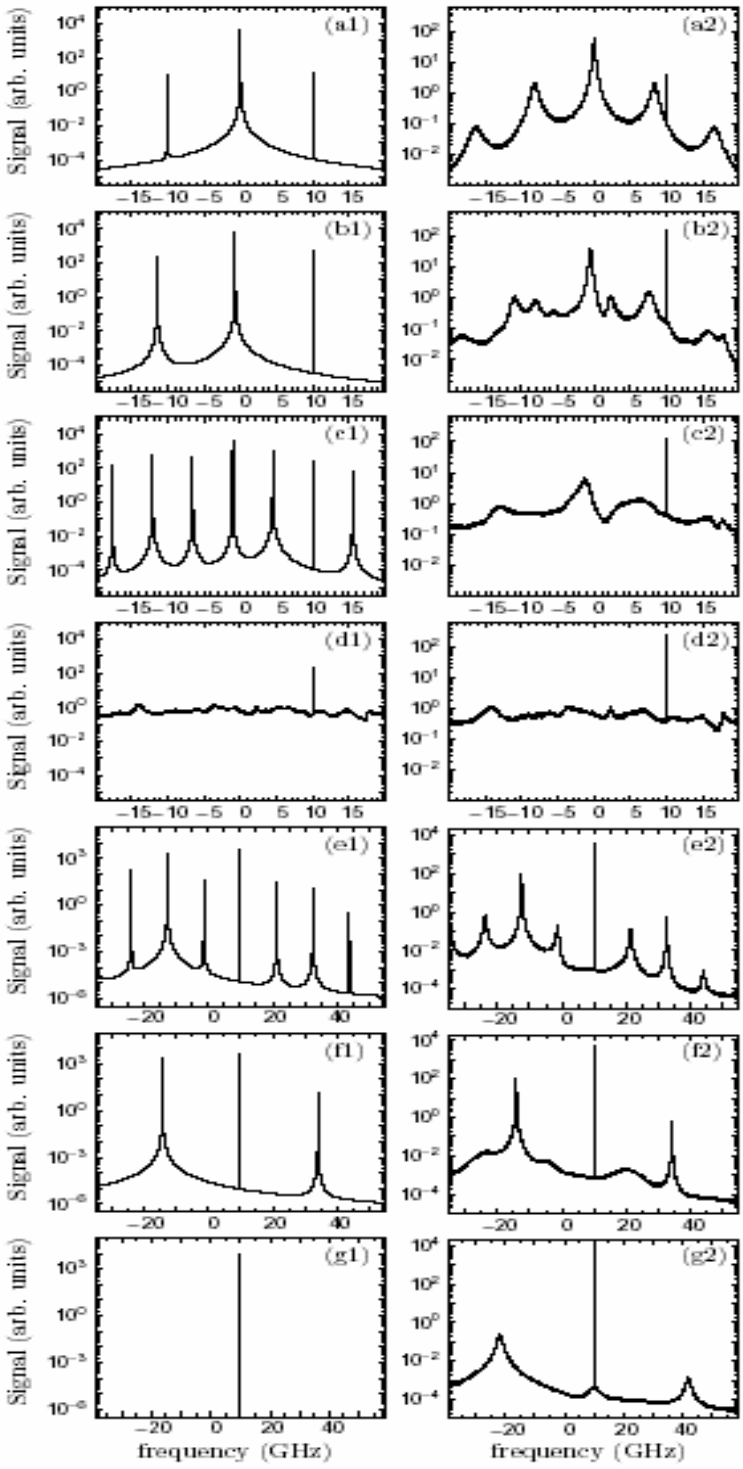

Fig. 6. Spectra for Laser A for noiseless (left column) and noisy (right column) cases. External signal intensities are (from top to bottom), 156 $\mu W/cm^2$, 15.6, 75.6, 160 mW/cm^2, 5, 7.6 and 25 W/cm^2. Also, $\Lambda/\Lambda_{th} = 2$ and $\Delta = 10$ GHz.

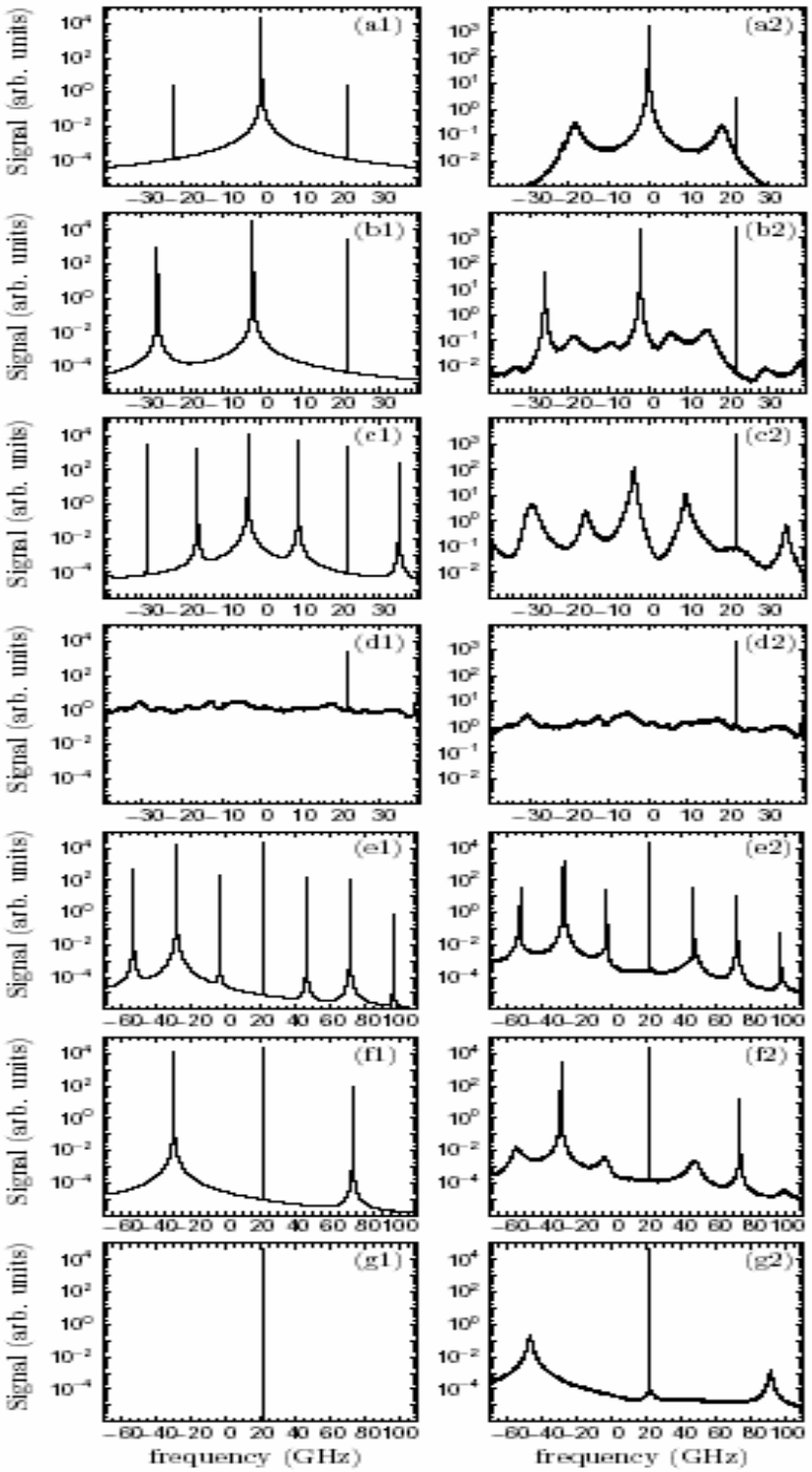

Fig. 7. Spectra for Laser A for noiseless (left column) and noisy (right column) cases. External signal intensities are (from top to bottom), 156 $\mu W/cm^2$, 563 mW/cm^2, 1.9, 4, 126.6, 156.3 and 625 W/cm^2. Also, $\Lambda/\Lambda_{th} = 6$ and $\Delta = 10$ GHz.

Focusing first on the noiseless case, we see that for external-signal intensities below the instability threshold, the power spectra consist of a peak at the injection-modified lasing frequency, a peak (detuned by Δ) at the injected field frequency, and a peak corresponding to its complex conjugate at $-\Delta$, that is due to four-wave mixing. As the external-signal intensity increases, the detector laser undergoes period doubling bifurcation, which is accompanied by the appearance of additional peaks halfway between the above mentioned peaks [Figs. 5 (b1), 6 (c1) and 7 (c1)]. Subsequent bifurcations lead to chaotic dynamics which manifests as a continuum of frequencies with no distinct spectral components (except for that of the injected field) [Figs. 5 (c1), 6 (d1) and 7 (d1)]. With further increase in external-signal intensity, inverse period-doubling bifurcations give arise to period-two oscillations [Figs. 5 (d1), 6 (e1) and 7 (e1)] and then to period-one oscillation [Figs. 5 (e1), 6 (f1) and 7 (f1)]. Finally, phase locking is achieved via Hopf bifurcation [Figs. 5 (f1), 6 (g1) and 7 (g1)].

The right columns of Figs. 5 – 7 show the effects of noise, e.g., from spontaneous emission. As expected, the influence of noise is the strongest close to threshold and decreases with increasing excitation. For example, in Fig. 5, which is for the low excitation of $\Lambda/\Lambda_{th} = 1.2$, the spectra in the left and right columns are significantly different. The difference indicates that the effect of noise is the washing out the detector-laser intensity peaks. Consequently, none of the bifurcations identified in the left column can be seen in the right column. However, noise effects involve more than the broadening of intensity peaks. Figure 6 shows that for $\Lambda/\Lambda_{th} = 2$, wave mixing can also result in the creation of satellite resonances [Fig. 6 (a2) and (b2)]. At higher external-signal intensity, period-doubling bifurcation becomes noticeable. Figure 7 for $\Lambda/\Lambda_{th} = 6$ indicates that noise effects on externally-induced instabilities become less important when one operates the detector laser further above threshold. Note that many of the noisy spectra in Figs. 6 and 7 contain features that are absent in the noiseless ones. These include excitation of otherwise damped resonances such as RO [(a2) and (g2)], wave mixing (b2), and anticipation of imminent bifurcations (f2).

B. Sensitivity to external signal noise

This subsection describes the effects of noise in the external signal by introducing $D_\varphi > 0$. Results are presented for Laser A operating with $\Lambda/\Lambda_{th} = 2$. If the external signal coherence time, $1/D_\varphi$ is much larger than the RO period of the detector laser, the detector laser field will adiabatically follow the external-signal fluctuations, and the net result is a smearing of the bifurcation boundaries, as may be seen by comparing Figs. 3 (a) and 8 (a). As the coherence time approaches the RO period, the phase fluctuations in the external signal interfere with the detector laser dynamics so that specific bifurcations can no longer be distinguished, but some features of the response to a coherent field remain, including the large-amplitude oscillations around $I_{ext} = 0.11$ W/cm² (see Figs. 8 (b) and 8 (c) for $D_\varphi/\pi = 1$ GHz and $D_\varphi/\pi = 10$ GHz, respectively). With further decrease in coherence, any indication of coherent injection phenomenon vanishes, as is the case for $D_\varphi/\pi = 10^3$ GHz shown in Fig. 8 (d).

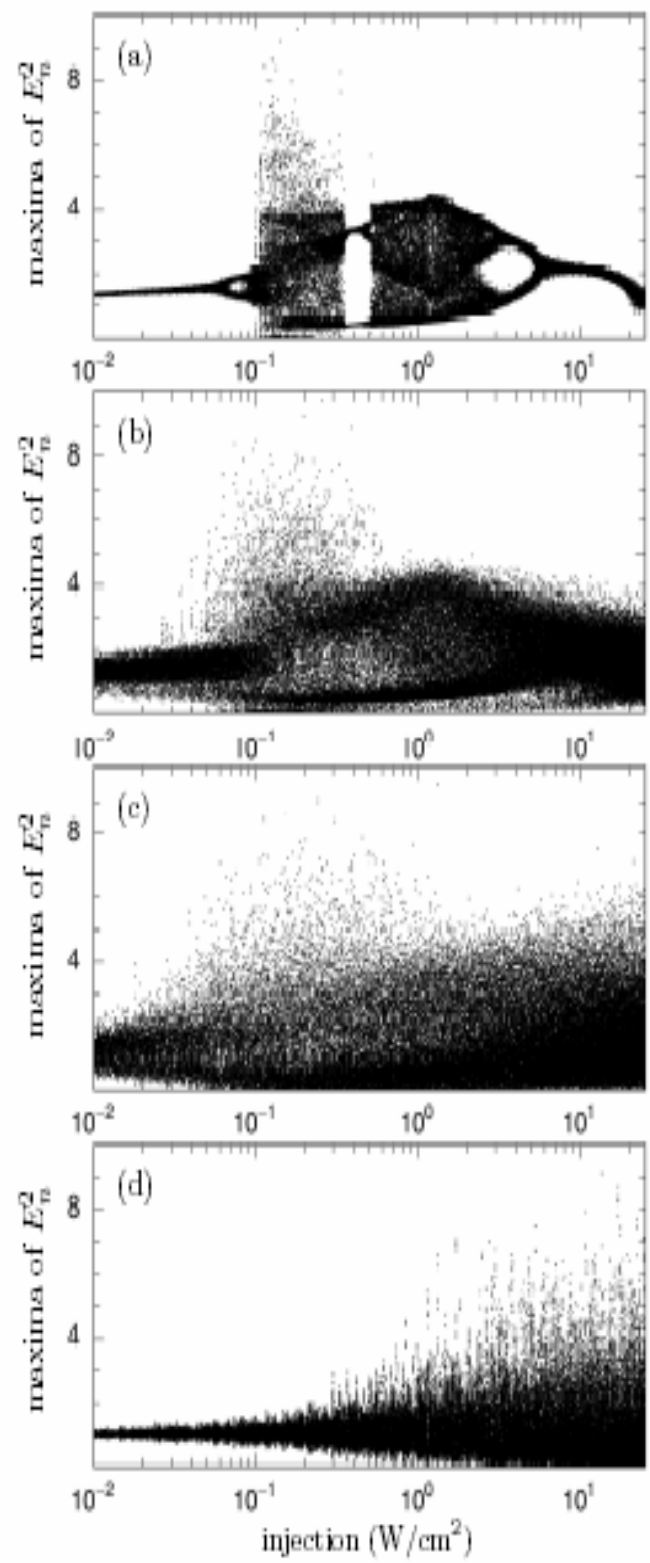

Fig. 8. Maxima of detector-laser intensity for Laser A with noisy external signal. $\Lambda/\Lambda_{th} = 2$ and $\Delta = 10$ GHz and $D_{\phi}./\pi = 0.01$, 1, 10 and 1000 GHz (top to bottom).

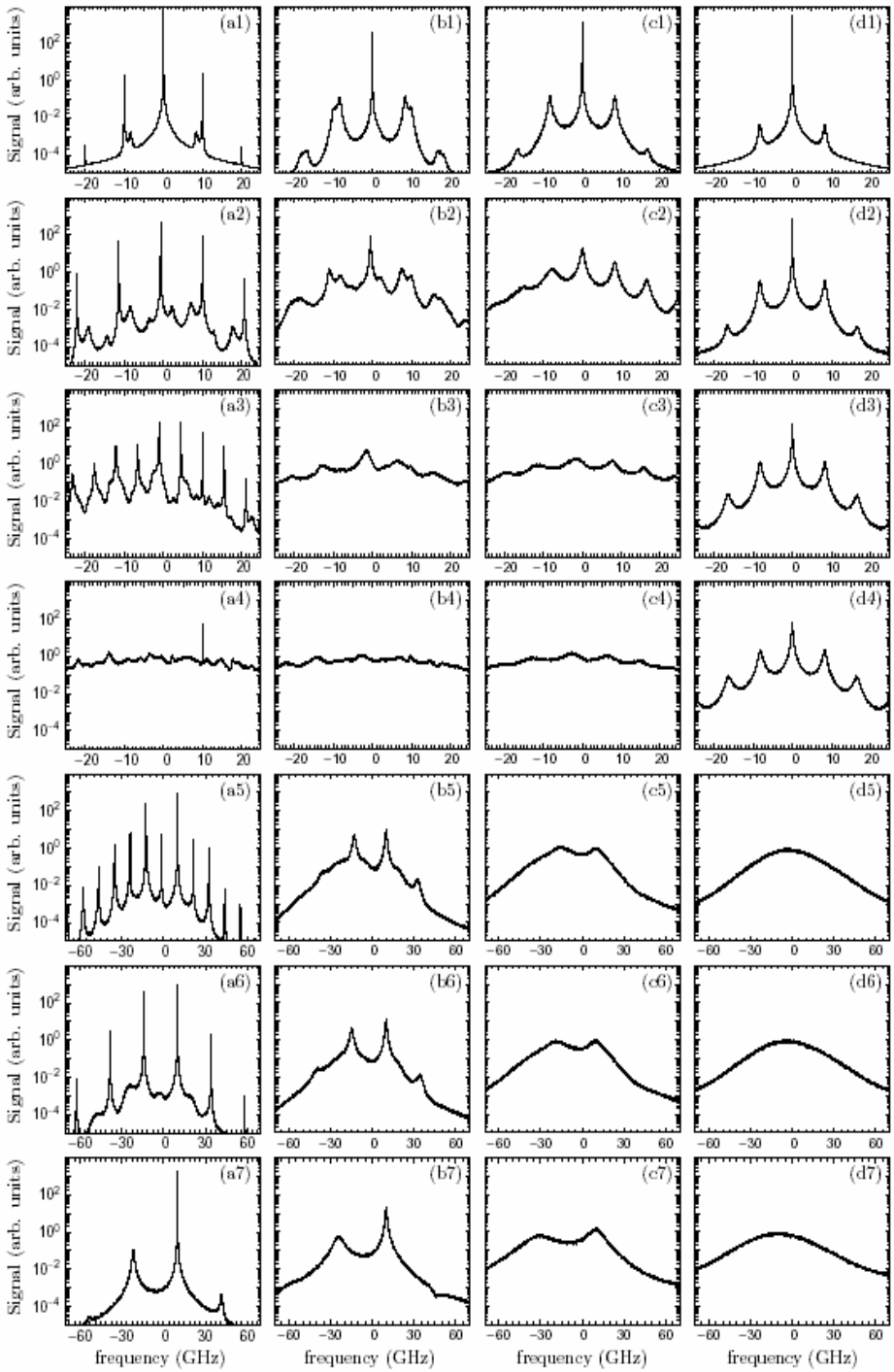

Fig. 9. Laser A spectra with noisy external signal, with $\Lambda/\Lambda_{th} = 2$ and $\Delta = 10$ GHz. External signal intensities are (from top to bottom), 156 $\mu W/cm^2$, 15.6, 75.6, 160 mW/cm^2, 5 and 25 W/cm^2. From (a) to (d), $D_\phi./\pi = 0.01$, 1, 10 and 1000 GHz.

More information on the effects of external signal noise may be obtained from the detector laser spectrum. Figure 9 shows the spectra, where each column is for a given D_φ, with D_φ increasing from left to right. Each row is for a fixed I_{ext}, with increasing I_{ext} from top to bottom. In term of the power spectrum, all bifurcations found for the coherent external signal are also clearly distinguishable for $D_\varphi/\pi = 0.01$ GHz [Fig. 9 (a1) – (a7)]. For $D_\varphi/\pi = 1$ GHz, the changes with increasing I_{ext} are still noticeable, but the bifurcations are no longer distinguishable [Fig. 9 (b1) – (b7)]. For $D_\varphi/\pi = 10$ GHz, most of the dynamical transitions shown in Figs. 9 (a1) – (a7) disappear and the system becomes less useful for detecting an external signal. This is because the spectrum evolves continuously from that of a noisy free-running laser to one showing a spectrally broad emission with broad peaks indicating the presence of the external signal and the injection-modified lasing mode [Fig. 9 (c5) – (c7)]. At $D_\varphi/\pi = 1000$ GHz, there is completely no resemblance Figs. 9 (a1) – (a7). Figure 9 (d1) - (d4) indicate that for low I_{ext}, external signal influence is similar to that of noise within the detector laser. For high I_{ext}, Figs. 9 (d5) – (d7) show a broad single intensity peak with FWHM of few tens of GHz, which is much larger than that of the free-running detector laser and much smaller than that of the external signal.

VI. Conclusion

This report describes work performed for a LDRD project on a quantum optical approach to detecting weak coherent radiation in the presence of a strong incoherent background. The approach is based on the extreme sensitivity of laser dynamical nonlinearities to the coherence of external perturbation. An externally-induced dynamical phase transition, e.g., between stable and chaotic operation, may be used to indicate the presence of coherent radiation. Stimulations performed on a baseline scheme, consisting of a semiconductor laser operating with a Fabry-Perot resonator, gave the following results.

1) With laser light injection, chaos occurs at injected intensity that is 6 orders of magnitude smaller than the detector-laser intracavity intensity, thus showing extreme sensitivity of scheme to external coherent radiation.
2) To induce chaos with incoherent light requires greater than 4 orders of magnitude higher intensity compared to laser light injection, thus assuring good discrimination between coherent and incoherent perturbations.
3) Chaotic regions are readily modifiable by changing excitation level, gain structure or optical resonator configuration, thus allowing optimization for specific detection mission.

The above results indicate that the scheme has potential to be viable in remote sensing applications, such as satellite laser threat warning receivers. We strongly recommend proceeding with a proof-of-principle experiment.

Some concerns remained, the most important being the difficulty in achieving a broad detection bandwidth. We recommend a follow-on study to explore incorporating a photonic lattice into the basic scheme. With photonic-lattice frequency bands instead of discrete Fabry-Perot resonances, it may be possible to improve detection bandwidth.

In terms of the broader goal of creating a technological base for supporting long term interests in RSVP, we have made the first steps in laying a foundation. The 1-year LDRD project has allowed the physics participants to better appreciate the LTWR mission, and hopefully provided the engineering participants a better appreciation of the relevant quantum technology. Additionally, we demonstrated the capability to evaluate in a timely manner the viability of specific quantum technology for a specific Sandia mission. We enthusiastically argue for the continuation of the activity of seeking opportunities for infusion of recent quantum technologies to the RSVP area.

References

1. B. Krauskopf and D. Lenstra (Eds.), *Fundamental Issues of Nonlinear Laser Dynamics*, AIP Conference Proceedings **548** (2000).
2. D.M. Kane and K.A. Shore (Eds.), *Unlocking Dynamical Diversity: Optical Feedback Effects on Semiconductor Lasers*, Wiley, 147 (2005).
3. S. Wieczorek, B. Krauskopf, T.B. Simpson, and D. Lenstra, "The dynamical complexity of optically injected semiconductor lasers," Phys. Rep. **416**, 1 (2005).
4. C.H. Henry, "Theory of the linewidth of semiconductor laser," IEEE J. Quantum Electron. **QE-18,** 259 (1982).
5. S. Wieczorek, B. Krauskopf and D. Lenstra, "A unifying view of bifurcations in a semiconductor laser subject to optical injection," Opt. Comm. **4172**, 279 (1999).
6. S.K. Hwang and J.M. Liu, "Dynamical Characteristics of an optically injected semiconductor laser", Opt. Comm. **183,** 195 (2000).
7. K.E. Chlouverakis and M.J. Adams, "Stability map of injection-locked laser diodes using the largest Lyapunov exponent," Opt. Comm. **216**, 405 (2003).
8. S. Wieczorek and W. W. Chow, "Global view of nonlinear dynamics in coupled-cavity lasers: a bifurcation study," Opt. Comm. **246,** 471 (2005).
9. W.A. van der Graaf, A.M. Levine and D. Lenstra, "Diode lasers locked to noisy injection," IEEE J. Quantum Electron. **QE-33**, 434 (1997).
10. S. Wieczorek, T. B. Simpson, B. Krauskopf, and D. Lenstra, "Global quantitative predictions of complex laser dynamics," Phys. Rev. E **65**, 045207(R) (2002).
11. S. Eriksson, "Dependence of the experimental stability diagram of an optically injected semiconductor laser on current injection," Opt. Comm. **210**, 343 (2002).
12. S. Wieczorek, T. B. Simpson, B. Krauskopf, and D. Lenstra, "Bifurcation transitions in an optically injected diode laser: theory and experiment," Opt. Comm. **215**, 125 (2003).
13. S. Valling, T. Fordell, and A.M. Lindberg, "Maps of the dynamics of an optically injected solid-state laser," Phys. Rev. A **72**, 033810 (2005)

Appendix I: Publication List

1. S. Wieczorek, W. W. Chow, L. Chrostowski, C. J. Chang-Hasnain, 'Improved semiconductor-laser dynamics from induced population pulsation,' IEEE Journ. Quantum Electron. **42**, 552 (2006).
2. S. Wieczorek and W. W. Chow, 'Self-induced chaos in a single-mode inversionless laser,' Phys. Rev. Lett. **97**, 113903 (2006).
3. L. Chrostowski, B. Faraji, W. Hofmann, M.-C. Amann, S. Wieczorek and W. W. Chow, '40 GHz bandwidth and 64 GHz resonance frequency in injection-locked 1.55 μm VCSELs,' (submitted to IEEE, Special Issue on Semiconductor Lasers).
4. S. Wieczorek and W. W. Chow, 'On the dynamical sensitivity of lasers and instability-based coherent-signal detectors,' (in preparation).
5. S. Wieczorek and W. W. Chow, 'Using chaos for ultrasensitive coherent signal detection,' (TA in preparation).

Improved Semiconductor-Laser Dynamics From Induced Population Pulsation

Sebastian Wieczorek, Weng W. Chow, Lukas Chrostowski, *Member, IEEE*, and Connie J. Chang-Hasnain, *Fellow, IEEE*

Abstract—**This paper investigates theoretically the modification of dynamical properties in a semiconductor laser by a strong injected signal. It is found that enhanced relaxation oscillations are governed by the pulsations of the intracavity field and population at frequencies determined by the injected field and cavity resonances. Furthermore, the bandwidth enhancement is associated with the undamping of the injection-induced relaxation oscillation and strong population pulsation effects. There are two limitations to the modulation-bandwidth enhancement: Overdamping of relaxation oscillation and degradation of flat response at low frequencies. The injected-laser rate-equations used in the investigation reproduce the relevant aspects of modulation-bandwidth enhancement found in the experiment on injection-locked vertical-cavity surface-emitting lasers.**

Index Terms—**Injection locking, modulation bandwidth, modulation response, population pulsation, relaxation oscillation, semiconductor lasers.**

I. Introduction

HIGH-SPEED semiconductor lasers are important for applications such as optical data transmission. The relaxation oscillation (RO) frequency provides an indication of modulation speed in these lasers [1]–[3]. A semiconductor laser exhibits damped relaxation oscillations because of a time dependent energy exchange between laser field and carrier population. RO frequency for free-running semiconductor lasers typically ranges from 1 to 20 GHz [4], [5].

An interesting discovery is that the RO frequency of a semiconductor laser may be appreciably increased with injection locking [1], [6]. The early observations were in index-guided quantum-well lasers [1] and distributed feedback (DFB) lasers [3]. Later experiments focused on external-cavity lasers [7] and vertical-cavity surface-emitting lasers (VCSELs), where a RO frequency exceeding 50 GHz was recently achieved [6]–[11]. Analytical studies [12] and numerical simulations using rate equation models were able to reproduce many aspects of the experimental results [1], [2], [13]–[16]. However, these simulations were unable to clearly identify the physical processes related to the dynamical response enhancement.

Given the good qualtitative agreement between theory and experiment (e.g., see Figs. 15 and 16) the injected-laser rate-equation model appears to contain the physics resulting in the observed dynamical behavior. The rate-equation model, introduced by Lang [17], consists of three coupled first-order ordinary differential equations describing the time evolution of laser field amplitude, laser phase and total carrier density. Terms are introduced to account for the effects of coherent field injection. This model is being used extensively and successfully to investigate injection locked semiconductor lasers.

The difficulties encountered by earlier studies in obtaining a comprehensive description and identifying important physical processes arise not from limitations of the rate-equation model but from the numerical approaches. By relying solely on simulations performed by numerically integrating the equations of motion, one cannot practically explore, in necessary detail, the broad range of physical parameters that can influence the laser dynamics. In this paper, we circumvent this difficulty by using a dynamical system approach that relies heavily on bifurcation theory and continuation techniques [18] (see also [19] and [20] for more details on bifurcation analysis in semiconductor laser systems). Bifurcation diagrams facilitate immensely the systematic search of the extensive parameter space to identify the important contributions. The continuation techniques supplement the direct time integration to enable each parametric study to be performed to the necessary detail and with relatively modest computational resources. As a result, we are able to identify important physical processes associated with modified RO (i.e., modified RO frequency and damping rate) and enhanced modulation bandwidth. Furthermore, we uncover limitations to this bandwidth enhancement approach.

Section II summarizes the rate equation model and Section III discusses the two types of transition to locking. In Section IV, we review the relaxation oscillation physics and discuss the role of injection-induced population pulsation in the modified RO process. Section V emphasizes the modifications to the link between RO frequency and damping by optical injection, presents the resulting enhancement in laser dynamical response, and discusses the physical processes associated with bandwidth enhancement. Also, it uncovers the limitations of the optical injection scheme. The extent to which the enhancement depends on injection conditions and different types of lasers, characterized, e.g., by different population-induced refractive index effects (Ω) [21] is also examined. A comparison between theory and experiments showing good agreement is presented in Section VI.

Manuscript received November 11, 2005; revised February 22, 2006. This work was supported in part by the U.S. Department of Energy under Contract DE-AC04-94AL8500.

S. Wieczorek and W. W. Chow are with Sandia National Laboratories, Albuquerque, NM 87185 USA (e-mail: smwiecz@sandia.gov; wwchow@sandia.gov).

L. Chrostowski is with the Electrical and Computer Engineering, University of British Columbia, Vancouver, BC V6T-1Z4, Canada (e-mail: lukasc@ece.ubc.ca).

C. J. Chang-Hasnain is with the Electrical Engineering and Computer Science Department, University of California, Berkeley, CA 94720-1770 USA (e-mail: cch@eecs.berkeley.edu).

Digital Object Identifier 10.1109/JQE.2006.874753

II. Theory

The injected-laser rate-equation model is based on semiclassical laser theory. By assuming a quasi-equilibrium condition and an active-medium polarization that adiabatically follows the time variations of the laser field and carrier population, the equations of motion describing system dynamics are

$$\dot{E} = \frac{c}{n_b}\Gamma\xi(N - N_{th})E + \frac{c\sqrt{T}}{2n_bL}E_i\cos\psi \quad (1)$$

$$\dot{\psi} = 2\pi\Delta - \alpha\frac{c}{n_b}\Gamma\xi(N - N_{th}) - \frac{c\sqrt{T}}{2n_bL}\frac{E_i}{E}\sin\psi \quad (2)$$

$$\dot{N} = \Lambda' - \gamma_N N - \frac{\epsilon_0 n_b c}{\hbar\nu}\left[g_{th} + \xi(N - N_{th})\right]E^2 \quad (3)$$

where E is the intracavity electric field amplitude, ψ is the phase difference between the injected and intracavity fields, and N is the total carrier density. According to the derivation by Spencer and Lamb [22], the injection of a coherent field, with amplitude E_i and frequency ν_i, introduces driving terms to the laser field equations of motion, as shown in (1), (2). Also, in the previous equations, the threshold local-gain and carrier-density in a free-running laser are

$$g_{th} = \frac{n_b\gamma_E}{2c\Gamma}$$

$$N_{th} = N_{tr} + \frac{n_b\gamma_E}{2c\Gamma\xi}$$

where N_{tr} is the transparency carrier density, Γ is the confinement factor, ξ is the differential gain, γ_E and γ_N are the photon and population decay rates, respectively, α is the linewidth enhancement factor, c is the speed of light in vacuum, n_b is the background refractive index, L is the cavity length, Δ is the detuning between injected and free-running laser frequencies, and T is the transmission of the laser mirror through which the light is injected. Anticipating the calculation of modulation response curves in Section V, we write the excitation rate as

$$\Lambda' = \Lambda\left[1 + \delta\sin(2\pi ft)\right] \quad (4)$$

where δ is the modulation depth and f is the modulation frequency.

Equations (1)–(3) assume single-mode operation, which is consistent with typical VCSEL or distributed feedback (DFB) laser operation. Phase fluctuations in the injected field are ignored because we assume that the injected signal comes from a master laser that is considerably more stable than the laser being studied (slave laser). Consequently, the slave laser field adiabatically follows any injected signal fluctuations [6]–[11], and the net result of these fluctuations is a smearing of the bifurcation boundaries. Most of our discussions involve locked operation sufficiently away from these boundaries [23], [25].

To facilitate the numerical computations, we introduce the normalized quantities

$$E_n = \frac{E}{E_0} \quad N_n = \frac{(N - N_{th})}{N_{th}}$$

$$\Lambda_n = \frac{\Lambda}{\Lambda_{th}} \quad K = \frac{c\sqrt{T}E_i}{2n_bL\gamma_N E_0}$$

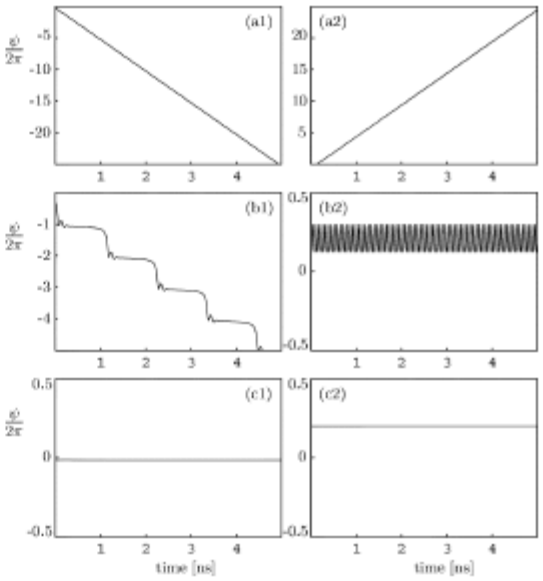

Fig. 1. Two columns show examples of the two types of locking transition for $\alpha = 2$ and $\Lambda_n = 2$. From (a1)–(c1): $\Delta = -5$ GHz and $K = 1.0, 7.3$, and 8.0. From (a2)–(c2): $\Delta = 5$ GHz and $K = 1, 35$, and 50.

where E_0 is the free-running laser intracavity-field at twice threshold, $\Lambda_{th} = \gamma_N N_{th}$ is the free-running laser threshold excitation rate, and K is the normalized injection strength.

The results in Figs. 1 and 3–14 are obtained for $N_{tr} = 10^{24}$ m^{-3}, $\Gamma = 0.05$, $\xi = 10^{-19}$ m^2, $\gamma_E = 5 \times 10^{11}$ s^{-1}, $\gamma_N = 2 \times 10^9$ s^{-1}, $n_b = 3.4$, and $\delta = 0.05$. To reproduce measurements in Figs. 15 and 16, we changed some of these parameters as indicated in the figure captions. Calculations presented in Figs. 3, 4 (c2), 5, 6, and 10–16 were obtained using the bifurcation continuation package AUTO [18].

III. Injection Locking

Dynamics of an injected laser described by (1)–(3) with $\Lambda' = \Lambda$ evolve in a three-dimensional (3-D) phase space. Unlocked operation is usually indicated by a stable periodic orbit (and sometimes by a non periodic attractor) that surrounds the origin of the complex $E^{i\psi}$ plane in the $\{\mathrm{Re}(Ee^{i\psi}), \mathrm{Im}(Ee^{i\psi}), N\}$ phase space. Injection locking is indicated by a stable stationary point of (1)–(3) and can be achieved in two distinct manners. We speak of two different types of transition to locking. (Note that in some cases with $\alpha \sim 0$ complicated dynamics near saddle-node-Hopf points gives rise to a third type of locking transition called period-adding cascade [27] which is not relevant for the problem considered here.) There are differences in the dynamics of E, ψ and N between these two types of locking transition, and we choose the dynamics of ψ to show their examples in Fig. 1.

The first type of locking transition involves steps (a1), (b1), and (c1) from Fig. 1. When a laser is unlocked, the phase difference ψ varies linearly in time (a1). As locking is approached,

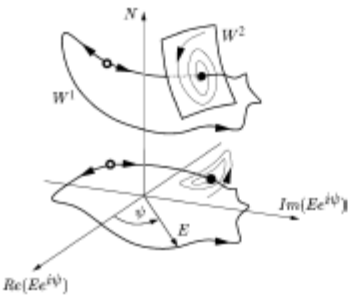

Fig. 2. Sketch of a typical phase portrait near the injection-locked stable stationary point (filled dot), and its projection onto the complex $Ee^{i\psi}$ plane. The two types of transition to injection-locking shown in Fig. 1 are associated with W^1 and W^2, respectively. The trajectories mark the time evolution of the tip of the $[\mathrm{Re}\langle Ee^{i\psi}\rangle, \mathrm{Im}\langle Ee^{i\psi}\rangle, N]$ vector in the direction indicated by the arrows, and an open dot marks the unstable point.

ψ varies in a step-like fashion (b1). It slows down when the right hand side of (2) approaches zero, giving rise to intervals of nearly constant $\dot{\psi}$, anticipating the imminent appearance of the stable stationary point. This process may also involve variations in the field-amplitude and population. Once locking is reached the period of the orbit goes to infinity. Such a type of locking transition is commonly referred to as Adler's locking [24]. In the 3-D phase space shown in Fig. 2, this type of locking transition is predominantly associated with the one-dimensional (1-D) W^1 which is initially the unlocked periodic orbit and after locking becomes tangent to the real eigenvector of the Jacobian of the system at the stable point. Here, locking occurs via global saddle-node bifurcation when stable and unstable stationary points appear on periodic orbit [26].

The second type of locking transition is illustrated by (a2), (b2), and (c2) from Fig. 1. It originates differently, with the active medium playing a role as explained in Section IV. Initially, the injected and laser fields are totally unlocked and their phase difference ψ increases linearly in time (a2). As the injection strength K increases, $\dot{\psi}$ becomes bounded and oscillates between $-\pi$ and π (b2). The periodic orbit no longer surrounds the origin of the complex $Ee^{i\psi}$ plane and always involves appreciable variations in the field-amplitude and population. The right-hand sides of (1)–(3) alternate in sign at the RO frequency producing sustained (by injection) RO with bounded phase. As the locking is approached, the amplitude of sustained RO decreases to zero and then the laser locks (c2). Such a type of locking transition, occurring in a reversed order, is often called RO undamping [28]. In the 3-D phase space shown in Fig. 2, RO undamping occurs predominantly in a two-dimensional (2-D) plane W^2 spanned by the two complex eigenvectors of the Jacobian of the system at the stationary point. Here, locking occurs via Hopf bifurcation when stable periodic orbit (sustained RO) shrinks onto unstable stationary point and the point turns stable.

The difference between the two types of locking transition that is crucial to our investigations is that RO undamping involves fast (GHz) oscillation [Fig. 1 (b2)]. In contrast, the oscillation frequency approaches zero in the first (Adler) type of locking transition [Fig. 1 (b1)]. This suggests that RO undamping rather than Adler locking is the key to understanding the improved high-speed performance of injected lasers, and we show in the following sections that this is indeed the case. Because the two types of locking transition manifest themselves as different bifurcations, we use bifurcation continuation techniques to guide us to the regions of enhanced laser dynamics in the parameter space. To this end, Fig. 3 repeats known results on the locking range in the (K, Δ) plane. The solid parts of Hopf (H) and saddle-node (S) bifurcation curves in Fig. 3 bound the locking region. The change in the type of locking transition is due to the codimension-two saddle-node-Hopf bifurcation points G which are also the origin of the complicated dynamics in injected lasers [29]. For $\alpha = 0$ the first and second type of locking transition take place at low and high K, respectively [Fig. 3(a)]. For $\alpha = 2$, the first and second type of locking transition take place at the lower and upper locking region boundary, respectively [Fig. 3(b)]. The details of the changes in the locking region with varying α are described in [26]. The rest of this paper focuses on portions of the locking region near the solid parts of Hopf (H) bifurcation where RO frequency and modulation bandwidth enhancement are present.

IV. Relaxation Oscillations in Injected Lasers

In the absence of an injected field and excitation modulation, i.e., $E_i = 0$, $\Lambda' = \Lambda$, the phase space reduces to $\{E, N\}$. When the excitation rate is abruptly increased from slightly below threshold to twice above threshold, the intracavity field E and population N of the free-running laser exhibit damped RO [Fig. 4 (a1–b1)]. The RO arise intrinsically because of the interplay of population buildup, stimulated emission and cavity decay. Until lasing threshold is reached, the population inversion increases at the rate $\Lambda - \Lambda_{th}$ [(3)], after which the field intensity builds up exponentially at the rate $2c\Gamma\xi(N - N_{th})/n_b$ through stimulated emission [(1)]. This causes the last term in (3) to become sufficiently large to deplete the population inversion to below its threshold value. Then, the field intensity decays because of the finite photon cavity lifetime. The process repeats itself until continuous wave operation is reached because of damping, as shown in Fig. 4 (a1) and (b1). From a small-signal analysis, we get two complex conjugate eigenvalues $-\gamma_{RO}^{fr} \pm i2\pi f_{RO}^{fr}$, where

$$\gamma_{RO}^{fr} = \frac{1}{2}\left[\gamma_N + \frac{2c\Gamma\xi}{n_b\gamma_E}(\Lambda - \Lambda_{th})\right] \tag{5}$$

$$f_{RO}^{fr} = \frac{1}{2\pi}\sqrt{\frac{2c\Gamma\xi}{n_b}(\Lambda - \Lambda_{th}) - \left(\gamma_{RO}^{fr}\right)^2} \tag{6}$$

are the RO damping rate and frequency, respectively. At twice threshold, $\gamma_{RO}^{fr} \simeq 3.8 \times 10^9\ \mathrm{s}^{-1}$ and $f_{RO}^{fr} \simeq 8.35$ GHz.

The second column in Fig. 4 shows that the laser dynamics is distinctly different in the presence of coherent-field injection. For the injection conditions stated in the figure caption, sustained RO arises via Hopf bifurcation [H in panel (c2)] for $\Lambda_{in} \gtrsim 2$, so that at $\Lambda_{in} = 2$ the laser is injection locked (c2). When the laser is perturbed away from the injection-locked stationary point (and off W^1) it exhibits damped RO. Although there is a decrease in the laser threshold due to injection (c2), the light intensity at $\Lambda_{in} = 2$ increases only by 7% over the free-running case. There is a slight 2% decrease in the average population inversion (b2), and hence in the stimulated emission

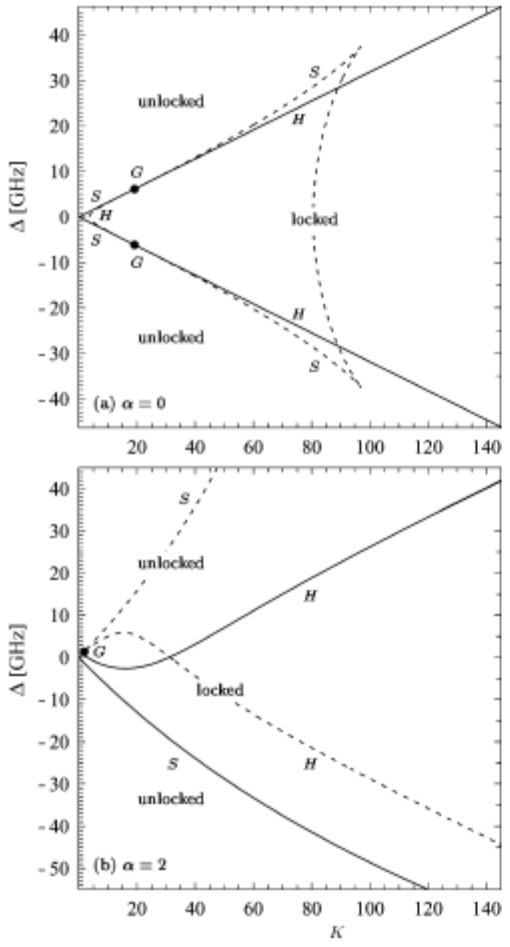

Fig. 3. Locking region in the $\langle K, \Delta \rangle$ plane is bounded by the supercritical parts (solid curves) of $\{S\}$ saddle-node and $\{H\}$ Hopf bifurcations. $\Lambda_n = 2$. The subcritical bifurcations of unstable solutions are shown as dashed curves. Bifurcation curves change from supercritical to subcritical at codimension-two saddle-node-Hopf points G.

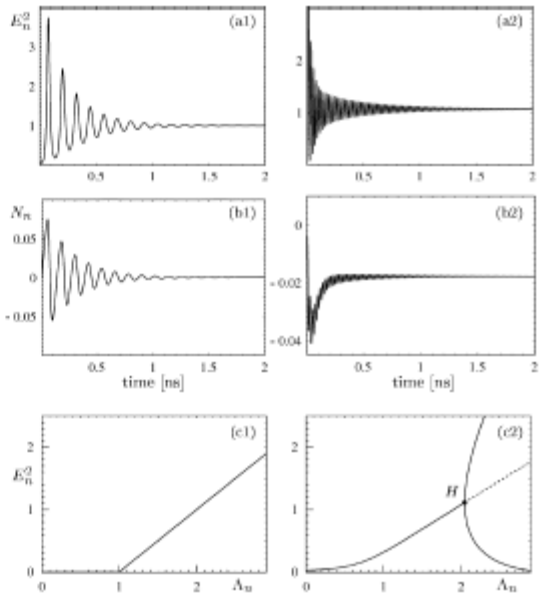

Fig. 4. [First column (a1–b1)] damped relaxation oscillation at $f_{RO}^{free} = 8.35$ GHz in a free-running laser and [second column (a2–b2)] damped relaxation oscillation at $f_{RO} = 42.4$ GHz in an injected laser for $\langle K, \Delta \rangle = \langle 135, 37.2\ \text{GHz} \rangle$. In both cases, $\alpha = 2$ and $\Lambda_n = 2$. Panels (c1) and (c2) show the dependence of laser intensity on the excitation rate. The two solid curves bifurcating from H in (c2) denote maximum and minimum of the oscillating field while the dashed curve indicates the unstable branch of stationary solution.

rate. In view of the lack of change in laser parameters, the question arises as to what physical processes are associated with the 500% increase in the rate of energy exchange between population and photons.

In Figs. 5 and 6, we show the RO frequency and RO damping rate of an injected laser for fixed K and varying Δ. The crosses correspond to a free-running laser. Notice that in Figs. (5b) and (6b), the γ_{RO} scale is nearly two orders of magnitude greater than the free-running laser value and the crosses appear at small positive γ_{RO}.

We first focus on the case of $\alpha = 0$ where (1)–(3) are symmetric with respect to the change $(\psi, \Delta) \rightarrow (-\psi, -\Delta)$. At fixed K, there is only one type of locking transition, and the change in the type of the locking transition occurs at $K \sim 20$ [Fig. 3(a)]. Weak injection barely influences the intrinsic resonance of a free-running laser [$K = 15$ in Fig. 5. However, at larger K, the RO process is significantly modified [$K = 115$ in Fig. 5]. On the one hand, as $|\Delta|$ approaches zero, damping of the RO increases to the point where the laser becomes overdamped [$K = 115$ and $-2.5\ \text{GHz} < \Delta < 2.5\ \text{GHz}$ in Fig. 5]. When RO frequency reaches zero, RO damping rate is no longer defined and hence the gap in the γ_{RO} curve for $K = 115$. On the other hand, for larger $|\Delta|$ and increasing K, we approach the solution $f_{RO} = |\Delta|$.

In semiconductor lasers, the variations in carrier population and optical frequency (chirp) are strongly coupled. This coupling is quantified by the linewidth enhancement factor α, and causes the cavity resonant frequency to shift due to injection-induced changes in the population density [(2)]. Therefore, there are qualitative differences in the case of $\alpha > 0$ as shown by comparing Figs. 5 and 6. First, semiconductor lasers respond differently to positively and negatively detuned injection signals, and have asymmetric locking ranges [Fig. 3(b)] [17], [26]. Fig. 6 shows the frequency and the damping rate of the RO for $\alpha = 2$. Because injection usually depletes the population, positive α causes decrease in the cavity resonant frequency, and the symmetric curves from Fig. 5(a), (b) shift toward the negative detuning and become distorted. Second, past the K value for the G^* point, there are two different types of locking transition at fixed K.

Under strong optical injection, the physical mechanisms that are responsible for RO in a free-running laser no longer apply.

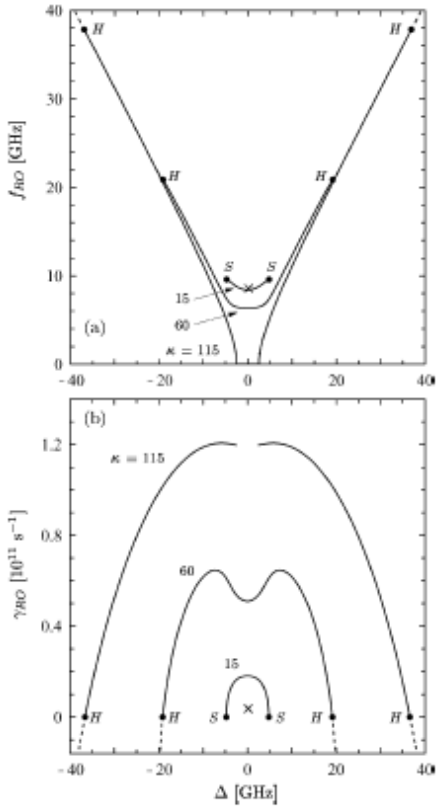

Fig. 5. (a) Relaxation oscillation frequency and (b) relaxation oscillation damping rate versus the injected light detuning for $\alpha = 0$, $\Lambda_{21} = 2$, and varying $K = 15, 60$, and 115. The stable locked solutions are in solid, and their boundaries due to (H) Hopf and (S) saddle-node bifurcations are marked with dots. Crosses correspond to a free-running laser. Compare the locking boundary with the supercritical bifurcation curves in Fig. 3(a).

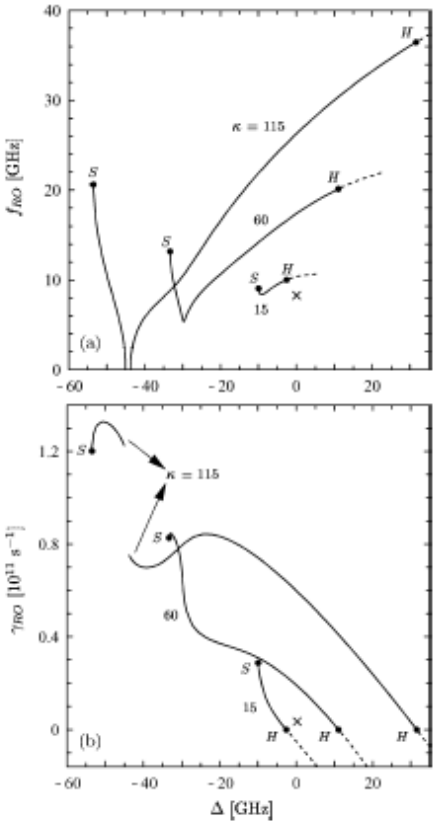

Fig. 6. (a) Relaxation oscillation frequency and (b) relaxation oscillation damping rate versus the injected light detuning for $\alpha = 2$, $\Lambda_{21} = 2$, and varying $K = 15, 60$, and 115. The stable locked solutions are in solid, and their boundaries due to (H) Hopf and (S) saddle-node bifurcations are marked with dots. Crosses correspond to a free-running laser. Compare the locking boundary with the supercritical bifurcation curves in Fig. 3(b).

On the one hand, if the injected field is nearly resonant with the cavity resonant frequency, the constructive interference between the two fields depletes the steady-state population, causing the stimulated emission rate to decrease. As a result, the electric field can no longer build-up quickly enough to deplete population below the already substantially depleted steady state level, and no repeated overshoot of the stationary state can occur. The RO become overdamped. On the other hand, if the injected field frequency is different from the cavity resonant frequency, after the injection-locked laser is perturbed away from the steady state (and off W^1), the total intracavity field oscillates at the beatnote between the injected and cavity-resonant frequencies [Fig. 4 (a2)]. This beatnote is the modified RO frequency [16]. Field oscillation induces population pulsation at the same frequency [Fig. 4 (b2)]. Population pulsation couples back to the field by interacting with the intracavity-field component at frequency ν_{ij} to modify the active-medium polarization at the cavity-resonant frequency [30].

It was recognized in [16] that, in strongly injected lasers, population pulsation amplitude may decrease by three orders of magnitude, and neglecting population pulsation leads to a correct value for the RO frequency. This result led to a conclusion that, under strong injection, population pulsation is negligible and plays no role in the RO process. Our findings show that: i) population pulsation remains nonnegligible at strong injection, and ii) its coupling back to the field may significantly modify the RO damping rate. [16] arrived at the opposite conclusions because it overlooked two facts: i) the significant decrease in the population pulsation amplitude is accompanied by a similar decrease in the field fluctuations, and ii) although population pulsation does not influence the RO frequency it may modify the RO damping rate. First, we show that population pulsation remains nonnegligible in strongly injected lasers, and then investigate its contribution to the RO process.

Fig. 7 shows the amplitude of sustained RO in injected laser without excitation modulation versus the normalized injection strength for $\alpha = 2$. For a given value of K, the data is taken for

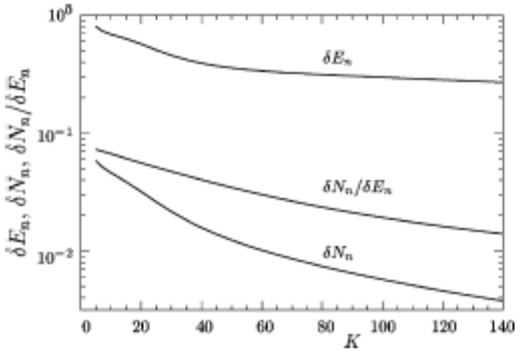

Fig. 7. Amplitude of sustained RO in the electric field (δE_n) and population (δN_n) vs. the normalized injection strength K, $\alpha = 2$, $\Lambda_n = 2$, and for given K the data is taken at 0.5 GHz past the locking boundary H (Hopf bifurcation).

sustained RO at 0.5 GHz above the supercritical Hopf bifurcation using

$$\delta E_n = \max(E_n) - \min(E_n)$$
$$\delta N_n = \max(N_n) - \min(N_n).$$

As the injection strength and detuning increase, the amplitude of population pulsation decreases faster than the amplitude of the electric field oscillation. From energy conservation arguments we conclude that the electric field pulsation is no longer entirely due to the energy exchange between the photons and electron-hole pairs. It becomes partially due to the beating between the two frequency components (one at ν_0 and the other at the cavity resonant frequency) of the intracavity field. However, $\delta N_n/\delta E_n$ decreases only by a factor of 5.3 over the range of injection strength $0 < K < 140$.

The RO process is quantified by its frequency f_{RO} and damping rate γ_{RO}. Population-pulsation contribution to the RO frequency and damping rate is obtained from

$$f_{RO}^{pp} = f_{RO} - \frac{1}{2\pi}\left[\Delta - \alpha\left(\frac{\gamma_E}{2} + \frac{c}{n_b}\Gamma\xi N_{tr}\right)N_n^{ss}\right] \quad (7)$$

$$\gamma_{RO}^{pp} = \gamma_{RO} - \left(\frac{\gamma_E}{2} + \frac{c}{n_b}\Gamma\xi N_{tr}\right)N_n^{ss}. \quad (8)$$

Here, f_{RO} and γ_{RO} are the exact RO frequency and damping rate, respectively, second terms on the right-hand sides are the RO frequency and damping rate, respectively, calculated with the neglect of population pulsation [16], and N_n^{ss} is the normalized population of the locked stationary state of (1)–(3). Fig. 8 shows f_{RO}^{pp} and γ_{RO}^{pp} at the locking transition H for $K = 140$ and varying α. In the range of $0 < \alpha < 7$ shown in the figure, we have $f_{RO}/f_{RO}^{pp} \sim 5$. Fig. 8(b) shows that f_{RO}^{pp} is only of the order of a few percent and is negligible. Consequently, f_{RO} remains near the beatnote between the injected and cavity-resonant frequencies [the second term on the right-hand side of (7)] [16]. However, γ_{RO}^{pp} can be large, up to ten times the RO damping rate of a free-running laser [Fig. 8(c)]. Furthermore, we find that there are two contributions to γ_{RO}^{pp}. The first contribution is the direct effect of population pulsation on

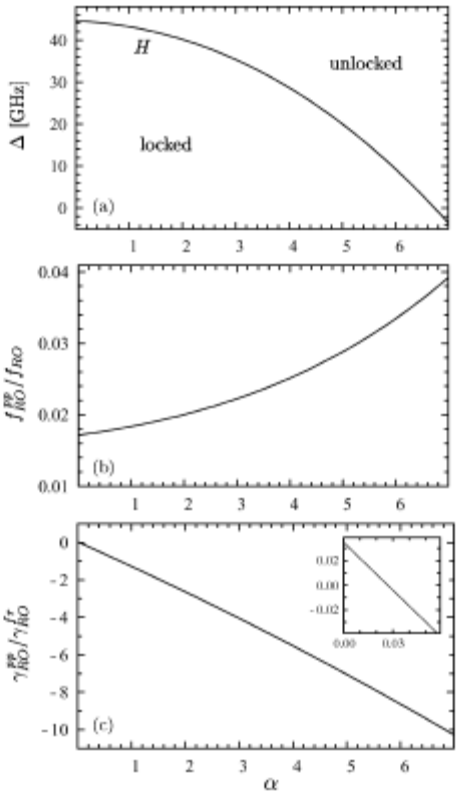

Fig. 8. (a) Locking boundary H (Hopf bifurcation) in the plane of the linewidth enhancement factor α versus injection detuning Δ for strongly injected lasers with $K = 140$ and $\Lambda_n = 2$. The corresponding contribution of population pulsation to the RO (b) frequency and (c) damping rate.

the active-medium polarization at the cavity-resonant frequency (population-field amplitude coupling). It results in additional cross-saturation of the field component at the cavity-resonant frequency [30] as indicated by a positive γ_{RO}^{pp} at $\alpha = 0$ [the inset in Fig. 8(c)]. Here, the direct effect is small because the beatnote between the injected and cavity resonant frequencies is much bigger than γ_N [30]. Second contribution, which is most significant, is the indirect effect of population-phase-amplitude coupling due to nonzero α. It depends on α and K, and, in contrast to the direct effect, results in reduced cross-saturation of the field component at the cavity-resonant frequency as indicated by decreasing γ_{RO}^{pp} in Fig. 8(c). This contribution vanishes when, for fixed K, the locking transition H occurs at similar Δ as it does for injected laser with the same K and $\alpha = 0$.

Population pulsation remains nonnegligible in strongly injected lasers and its effect on the RO process can be neglected only under conditions where both contributions to γ_{RO}^{pp} vanish or cancel each other. Some confusion may arise because the term "strong injection" is relative. In theory, there is always a sufficiently large K for which population pulsation is negligible. However, our calculations show that in typical strong-injection experiments ($2 < \alpha < 6$), such as those discussed in

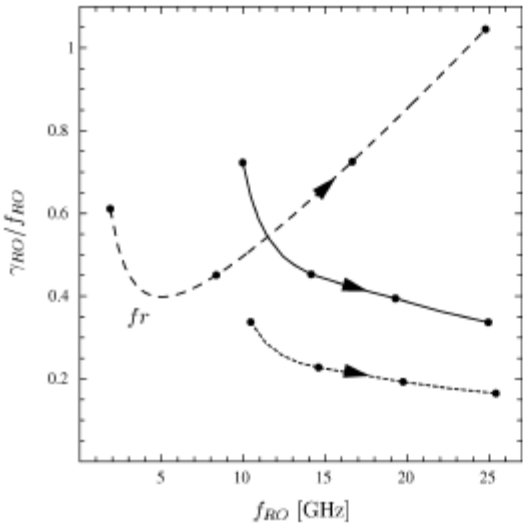

Fig. 9. (dashed) The intrinsic link between f_{RO} and γ_{RO} in a free-running semiconductor laser with $\alpha = 2$. The arrow indicates increasing excitation rate. From left to right the dots denote $\Lambda_{in} = 1.05, 2, 5,$ and 10. (solid and dotted) Different ways to adjust the relation between f_{RO} and γ_{RO} in an injected laser with $\Lambda_{in} = 2$ and $\alpha = 2$. The arrows indicate increasing detuning and from left to right the dots denote (solid) combinations of (K, Δ) taken 4 GHz below H (20, −6.4 GHz), (40, −0.9 GHz), (60, 7.1 GHz), and (80, 15.9 GHz), and (dotted) combinations of (K, Δ) taken 2 GHz below H (20, −4.4 GHz), (40, 1.1 GHz), (60, 9.1 GHz), and (80, 17.9 GHz).

Section VI, the RO damping rate is significantly decreased because of population pulsation. Neglecting population pulsation would lead to a much higher RO damping rate and suppression of the RO phenomenon.

V. Modulation Response

Laser modulation response is one factor affecting overall performance of an optical communication system [9]. Generally, a broad modulation bandwidth requires a combination of high f_{RO} and low γ_{RO}. A common practice to increase f_{RO} is by operating the laser further above threshold [31]. Unfortunately, f_{RO} and γ_{RO} are intrinsically linked in a free-running laser, such that any increase in f_{RO} is also accompanied by a greater increase in γ_{RO}. The problem is depicted by the dashed curve in Fig. 9, which is obtained by using (5), (6) and varying Λ_{in} from 1.05 to 10. The curve shows that while the ratio γ_{RO}/f_{RO} initially decreases with increasing f_{RO}, the trend reverses at higher f_{RO}. For the laser configuration considered, γ_{RO} eventually increases faster with increasing Λ_{in} than f_{RO}, after reaching a relaxation frequency of $f_{RO} = 5$ GHz with $\Lambda_{in} \approx 1.4$. A large γ_{RO} degrades the ability of the laser output to respond to the amplitude variations of the injection current.

Numerical continuation of injection-locked stationary point of (1)–(3) shows that the link between f_{RO} and γ_{RO} can be broken by taking advantage of the extra degrees of freedom provided by coherent optical injection. In most cases, optical injection increases γ_{RO}, and this may be seen in Figs. (5b) and (6b). However, for some combinations of injection strength and detuning (K and Δ, respectively), f_{RO} can be made to increase,

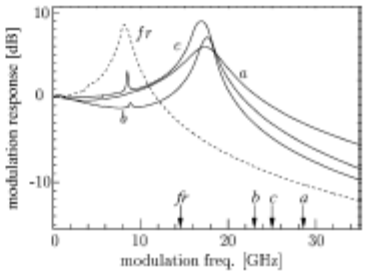

Fig. 10. Modulation response of weakly injected laser with $K = 50$. The combinations of $(\alpha, \Delta) =$ (a) (0.0,15.3 GHz), (b) (1.0, 12.7 GHz), and (c) (4.0, −16 GHz). The dashed curve is for the free-running laser. $\Lambda_{in} = 2$ and the arrows indicate the corresponding bandwidths.

while γ_{RO} remains constant or even decreases slightly. Such combinations exist, for example, in the neighborhood of bifurcation points H as shown in Fig. 5(a) and (b), as well as Fig. 6(a) and (b). The solid and dotted curves in Fig. 9 show this property. For each curve, the excitation is kept at $\Lambda_{in} = 2$, f_{RO} is increased by increasing K, while the ratio γ_{RO}/f_{RO} is decreased by adjusting Δ. For the solid and dotted curves, the combinations of K and Δ are chosen so that the laser maintains operation inside the locking region, at 4 and 2 GHz respectively, below the locking boundary H [cf. Fig. 3(b)].

To illustrate the actual improvement in modulation bandwidth, we perform numerical continuation of periodic orbit of (1)–(4) which represents a response of injection-locked laser to excitation modulation, for a range of modulation frequencies, using the excitation rate $\Lambda_{in} = 2$, with a small modulation depth of $\delta = 0.05$. Figs. 10–12 and (14a) are plots of normalized modulation response

$$10 \log_{10} \frac{\max\left[E_{in}^2(\omega)\right] - \min\left[E_{in}^2(\omega)\right]}{\max\left[E_{in}^2(1\text{ MHz})\right] - \min\left[E_{in}^2(1\text{ MHz})\right]}$$

as a function of modulation frequency f for different injection conditions and linewidth enhancement factors. In the presence of optical injection, the detuning is adjusted so that the injected laser operates within the stable locking range and near the supercritical part of Hopf bifurcation, where γ_{RO} approaches zero. From the modulation response curve, one can extract the modulation bandwidth, which is the modulation frequency where the modulation response is 3-db below the low-frequency response.

Fig. 10 depicts the results for weak injection ($K = 50$). Comparison of the dashed and solid curves indicates roughly a factor of 2 increase in f_{RO} with optical injection. (f_{RO} is located by the largest peak in the modulation response curve.) The different solid curves show that this increase in f_{RO} is insensitive to the linewidth enhancement factor α. Correspondingly, the laser modulation bandwidth is also increased over the free-running value. Curves a and fr in Fig. 10 show a two-fold improvement for $\alpha = 0$. As α increases slightly above zero, the improvement deteriorates and reaches a minimum around $\alpha \lesssim 1$ b. Thereafter, the modulation bandwidth resumes its increase with increasing α c.

Fig. 11 plots the modulation response for strong injection ($K = 140$). We see roughly a five-fold increase in f_{RO} with

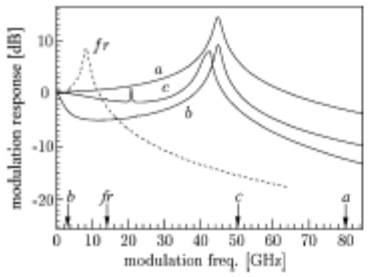

Fig. 11. Modulation response of strongly injected laser with $K = 140$. The combinations of $(\alpha, \Delta) =$ (a) (0.0,44 GHz), (b) (0.1, 44 GHz), and (c) (6.0, 7 GHz). The dashed curve is for the free-running laser. $\Lambda_n = 2$ and the arrows indicate the corresponding bandwidths.

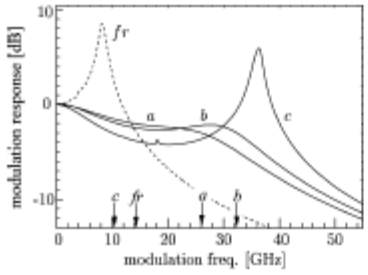

Fig. 12. Modulation response of strongly injected laser with fixed $K = 115$, $\alpha = 2$, and increasing $\Delta =$ (a) 0.0, (b) 10.0, and (c) 29.9 GHz. The dashed curve is for the free-running laser. $\Lambda_n = 2$ and the arrows indicate the corresponding bandwidths.

optical injection, for $0 \leq \alpha \leq 6$. However, as was pointed out in [12], the higher f_{RO} does not necessarily result in a broader modulation bandwidth. While the modulation response curve for $\alpha = 0$ *a* shows an approximately five-fold increase in the modulation bandwidth relative to that of the free-running laser, the $\alpha = 0.1$ modulation response curve with roughly the same f_{RO} shows a modulation bandwidth that is appreciably less. The reason for this anomaly is the significant degradation in low-frequency modulation response in the latter, as can be clearly seen in Fig. 11 *b*. For $\alpha > 0.1$, the low-frequency response gradually recovers, resulting in a flatter modulation response of the laser as can be seen in curve *c*.

We now identify processes associated with bandwidth enhancement in strongly injected semiconductor lasers. Fig. 13 presents the field and carrier modulation response for $K = 140$, and Fig. 14 shows two examples of the time evolution for the laser variables. At low modulation frequencies (first column in Fig. 14), the laser field amplitude, phase, and population (solid curves) closely follow variations in the locked solution arising from the excitation modulation (dashed curves). However, at higher modulation frequencies (second column in Fig. 14) where the bandwidth enhancement occurs, the laser field amplitude, phase, and population can no longer follow variations in the locked solution arising from the excitation modulation. Rather, the laser exhibits injection-sustained RO as it tries to converge to the fast-varying injection-locked solution. Figs. 13 *b* and 14 (c2) show that injection-induced population

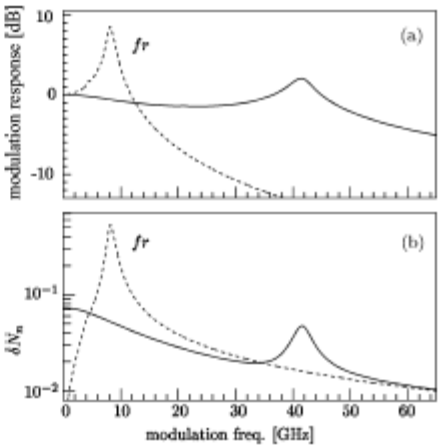

Fig. 13. (Solid) Modulation response of the (a) electric field and (b) population for $K = 140$, $\Delta = 62$ GHz, $\alpha = 4$, and $\Lambda_n = 2$. The dashed curves are for the free-running laser.

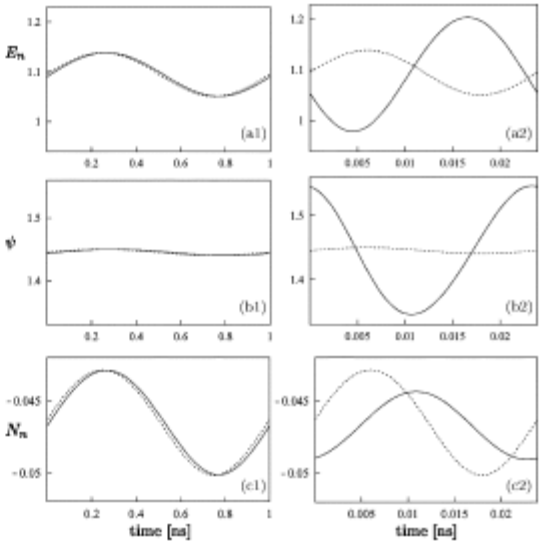

Fig. 14. (Dotted) Variations of the stable locked solution of (1)–(3) and (solid) the actual variations of (a) the normalized laser field amplitude, (b) phase difference, and (c) normalized population with excitation modulation at frequency of (first column) 1 GHz and (second column) 42 GHz; compare with Fig. 13. The solid curves are the stable limit cycles of the modulated laser, and $K = 140$, $\Delta = 62$ GHz, $\alpha = 4$, and $\Lambda_n = 2$.

pulsation is indeed present in enhanced modulation response. Furthermore, results in Figs. 8 and 11 show the relation between population pulsation and bandwidth enhancement. While strong laser-response at high frequencies is present in all curves in Fig. 11, the flat response at low frequencies which is also necessary for bandwidth enhancement occurs for parameters where there is strong population pulsation contribution to the RO damping rate; compare curve *c* in Fig. 11 with the bottom

panel in Fig. 8. We checked that the same is true for fixed α and varying K and Δ. (Notice that there is a significant bandwidth enhancement for $\alpha = 0$ where population pulsation contribution to the RO damping rate is vanishing. However, the absolute modulation response for $\alpha = 0$ is up to two orders of magnitude smaller than for $3 < \alpha < 6$. This difference cannot be seen from the plots of the normalized modulation response in Fig. 11 but will be discussed in our future work.)

One should be careful when studying excitation-modulation of initially locked laser because the locking boundary depends on N' and shifts in the (K, Δ) plane with varying excitation. We observed periodic response and modulation enhancement when the laser remained inside the locking region for all time and also in the cases where excitation modulation led to switching between locked and unlocked operation in the (K, Δ) plane. Whether the similar is true for large modulation depths remains an interesting question for future research. Excitation modulation of initially unlocked laser results in quasi-periodic operation that represents beating between sustained RO and modulation signal, and may sometimes lead to phase locking [33], [34].

We end this section by examining some of the features present in the curves in Figs. 10 and 12. First, we note that lasers with $\alpha = 0$ appears to benefit most from strong optical injection: One achieves significant modulation bandwidth increase without degradation of flat modulation response at low frequency. However comparison of curves a and b in Fig. 11 indicates that dynamical behavior of strongly injected laser is extremely sensitive to the slightest deviation from $\alpha = 0$. The low-frequency degradation can negate the benefits of strong optical injection in terms of increasing f_{RO} and limiting the growth of γ_{RO}. This is clearly illustrated in Fig. 12 where we plotted the modulation response for a laser with $\alpha = 2$ and $K = 115$. The different curves a to c correspond to increasing detuning, toward the Hopf bifurcation point. Despite the fact that f_{RO} increases and its resonance becomes more pronounced, which indicates a decreasing γ_{RO}, one obtains a narrower modulation bandwidth when going from curve b to c. The second feature involves the presence of other resonances in the curves of Figs. 10–12. These resonances are generated by the nonlinear active medium of the laser and are subharmonics of the relaxation oscillation frequency, i.e., they occur at frequencies $\{f_{RO}/q$, where $q = 1, 2, 3, \ldots$ [32]. Quite noticeable in Fig. 10 b, c, 11 c, and 12 c is the $q = 2$ contribution. Close examination reveals the $q = 3$ contribution in Figs. 10 c and 11 c.

VI. Comparison With Experiments

In this section, we show that it is possible to reproduce the most important features of the injection-locked modulation experiments performed with VCSELs using the injected-laser rate-equation model given by (1)–(4).

Figs. 15 and 16 show that we can achieve agreement for very different VCSEL structures. The difference is illustrated by a different low-frequency response with respect to the free-running laser response in the top panels of Figs. 15 and 16. Our calculations suggest that the VCSEL from Fig. 15 has a higher Q cavity, shorter carrier lifetime and, in particular, higher α than

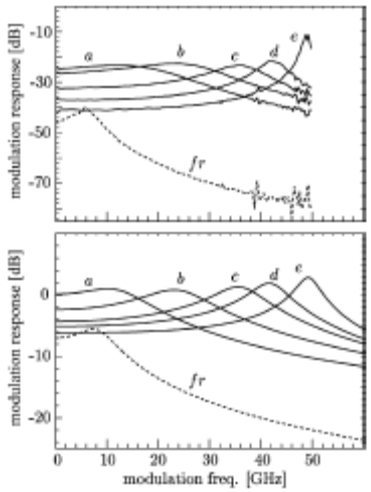

Fig. 15. (Top) Experimental modulation response of a VCSEL with injection ratio of 13.8 dB and detuning of $\Delta =$ (a) -156.1, (b) -79.7, (c) -14.2, (d) 31.7, and (e) 39.0 GHz; see [6] for more details on the experiment. (Bottom) theoretical modulation response for injection ratio of $20\log_{10}[E_i/(\sqrt{T}E_0)] = 15.2$ dB and $\Delta =$ (a) -26.3, (b) -14.3, (c) -1.6, (d) 5.6, and (e) 15.9 GHz. We used $K = 135$, $T = 0.004$, $L = 1.5$ μm, $\gamma_E = 8 \times 10^{10}$ s^{-1}, $\gamma_N = 5 \times 10^9$ s^{-1}, $\Gamma = 0.03$, $\alpha = 6$, $\Lambda_n = 2$, and other parameters as given in the last paragraph of Section II. Dashed curves are for free-running lasers.

the VCSEL from Fig. 16. This results in lower RO frequency and stronger RO damping rate for the free-running VCSEL from Fig. 15, and subsequently, in the stronger modulation response enhancement above the free-running laser response for injected VCSEL from Fig. 15. (We checked that the appreciable difference in the low-frequency modulation-response of the two lasers is not due to the different injection ratio.) Under strong optical injection, in both lasers, for a positive frequency detuning, very-high frequency relaxation oscillations were observed (up to 50 GHz) with a low damping (curves d and e). For a negative frequency detuning, high damping rates were observed leading to a flat frequency response (curves a and b). The linewidth enhancement factor for this type of VCSELs was measured in the range $4 < \alpha < 7$ [35] which is consistent with absence of the degradation of flat response at low frequencies. More details on the experiment can be found in [6], [10], and [11].

The bottom panels of Figs. 15 and 16 show unnormalized modulation response $10\log_{10}\{\max[E_n^2(\omega)] - \min[E_n^2(\omega)]\}$ obtained with (1)–(4) for the parameters given in the captions. Because of the uncertainty in measured values of the detuning and injection strength we treated Δ and K as a free parameters, adjusted to match the RO resonance peaks from the experiment. The theoretical curves reproduce well the trend across the locking range from weakly damped oscillations at a positive detuning to strongly damped oscillations with flat response at a negative detuning. In particular, we achieved good agreement in the modulation-response increase above the free-running laser response.

There are two discrepancies concerning the theoretical and experimental results. First is the difference in the values of Δ and K, and second is the strength of the response near the

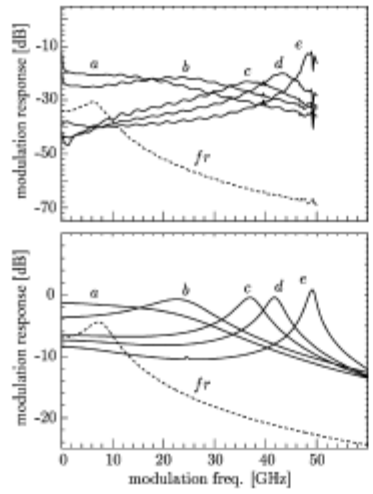

Fig. 16. (Top) experimental modulation response of a VCSEL with injection ratio of 12.5 dB and detuning of $\Delta =$ (a) -220.2, (b) -85.9, (c) -5.0, (d) 19.2, (e) 36.9 GHz; see [6] for more details on the experiment. (Bottom) theoretical modulation response for injection ratio of $20\log_{10}|E_i/\langle\sqrt{T}E_0\rangle| = 10.6$ dB and $\Delta =$ (a) -49.7, (b) -7.6, (c) 14.0, (d) 22.3, and (e) 35.0 GHz. We used $K = 100$, $T = 0.004$, $L = 1.5$ μm, $\gamma E = 1 \times 10^{11}$ s^{-1}, $\gamma N = 4 \times 10^{9}$ s^{-1}, $\Gamma = 0.03$, $\alpha = 4$, and other parameters as given in the last paragraph of Section II. Dashed curves are for free-running lasers.

RO resonance. The differences between theoretical and experimental values of Δ and K can be explained by approximations of the model (e.g. population independent $\tilde{\alpha}$) and large enough experimental uncertainties. Also, the theory underestimates the response at RO resonance for the far positive frequency detuning (curves *e* in Figs. 15 and 16) and overestimates the response at RO resonance for the far negative frequency detuning (curves *a* and *b* in Fig. 15 and curves *b* and *c* in Fig. 16). This difference is currently under investigation.

Equations (1)–(4) should also be applicable to DFB lasers. However, DFB lasers have smaller than VCSELs frequency separation between longitudinal modes which results in a narrower band for single-mode operation. Also, owing to the device geometry, it is harder to achieve high injection rates in DFB lasers.

VII. Conclusion

This paper analyzes the recent experimental observations of improvement in laser dynamical properties by coherent optical injection. We show that the experimental results can be accurately described by the widely used injected-laser rate-equation model, involving only three coupled ordinary differential equations. To better understand the phenomenon, bifurcation theory and continuation techniques are used to explore a wide range of experimental situations involving different injection conditions and laser types. The results clearly show different relaxation oscillation behaviors for free-running and injected lasers, arising from distinctly different physical processes. In contrast to the more familiar free-running or weak-injection configurations, the relaxation oscillation process in the presence of strong optical injection is governed by the pulsations of the intracavity field and population at frequencies determined by the injected field and cavity resonances. The appreciable bandwidth enhancement in strongly injected semiconductor lasers is found under conditions where the injection-induced relaxation oscillation: i) have its damping rate significantly decreased by the population pulsation, and ii) become undamped with the excitation modulation. The investigation also uncovers two factors limiting the bandwidth enhancement. They are degradation of low frequency response and overdamping of relaxation oscillation, for positive and negative detunings, respectively.

Acknowledgment

S. Wieczorek would like to thank T. B. Simpson for useful comments. W. W. Chow would like to acknowledge support from the Senior Scientist Award of the Alexander von Humboldt Foundation.

References

[1] T. B. Simpson, J. M. Liu, and T. B. Gavrielides, "Bandwidth enhancement and broadband noise reduction in injection-locked semiconductor lasers," *IEEE Photon. Technol. Lett.*, vol. 7, no. 7, pp. 709–711, Jul. 1995.

[2] T. B. Simpson and J. M. Liu, "Enhanced modulation bandwidth in injection-locked semiconductor lasers," *IEEE Photon. Technol. Lett.*, vol. 9, no. 10, pp. 1322–1324, Oct. 1997.

[3] X. J. Meng, T. Chau, and M. C. Wu, "Experimental demonstration of modulation bandwidth enhancement in distributed feedback lasers with external light injection," *Electron. Lett.*, vol. 34, pp. 2031–2032, Oct. 1998.

[4] X. Jin and L. Chuang, "Microwave modulation of a quantum-well laser with and without external optical injection," *IEEE Photon. Technol. Lett.*, vol. 13, no. 7, pp. 648–650, Jul. 2001.

[5] W. Kaiser, L. Bach, J. P. Reithmaier, and A. Forchel, "High-speed coupled-cavity injection grating lasers with tailored modulation transfer functions," *IEEE Photon. Technol. Lett.*, vol. 16, no. 9, pp. 1997–1999, Sep. 2004.

[6] L. Chrostowski, X. Zhao, C. J. Chang-Hasnain, R. Shau, M. Ortsiefer, and M.-C. Amann, "50 GHz optically injection-locked 1.55 μm VCSELs," *IEEE Photon. Technol. Lett.*, vol. 16, no. 2, pp. 367–369, 2006.

[7] Y. Okajima, S. K. Hwang, and J. M. Liu, "Experimental observation of chirp reduction in bandwidth-enhanced semiconductor lasers subjectto strong optical injection," *Opt. Commun.*, vol. 219, pp. 357–364, Apr. 2003.

[8] L. Chrostowski, C. H. Chang, and C. J. Chang-Hasnain, "Injection-locked 1.55 μm VCSEL's with enhanced spur-free dynamic range," *Electron. Lett.*, vol. 38, pp. 965–967, Aug. 2002.

[9] C. H. Chang, L. Chrostowski, C. J. Chang-Hasnain, and W. W. Chow, "Study of long-wavelength VCSEL-VCSEL injection locking for 2.5 Gb/s transmission," *IEEE Photon. Technol. Lett.*, vol. 14, no. 11, pp. 1635–1637, Nov. 2002.

[10] L. Chrostowski, W. Zhao, C. J. Chang-Hasnain, R. Shau, M. Ortsiefer, and M. C. Amann, "Very High Resonance Frequency (>40 GHz) optical injection-locked 1.55 μm VCSELs," in *Proc. IEEE Int. Topical Meeting on Microwave Photonics—Tech. Dig. MWP*, Oct. 2004, pp. 255–258.

[11] L. Chrostowski, X. Zhao, and C. J. Chang-Hasnain, "Microwave performance of optically injection-locked VCSELs," *IEEE Trans. Microw. Theory Tech.*, vol. 54, no. 2, pp. 788, 796, Feb. 2006.

[12] T. B. Simpson, J. M. Liu, and A. Gavrielides, "Small-signal analysis of modulation characteristics in a semiconductor laser subject to strong optical injection," *IEEE J. Quantum Electron.*, vol. 32, no. 8, pp. 1456–1468, Aug. 1996.

[13] J. M. Liu, H. F. Chen, X. J. Meng, and T. B. Simpson, "Modulation bandwidth, noise, and stability of a semiconductor laser subject to strong injection locking," *IEEE Photon. Technol. Lett.*, vol. 9, no. 10, pp. 1325–1327, Oct. 1997.

[14] R. J. Jones, P. S. Spencer, and K. A. Shore, "Influence of detuned injection locking on the relaxation oscillation frequency of a multimode semiconductor laser," *J. Mod. Opt.*, vol. 47, pp. 1977–1986, Sep. 2000.

[15] H. F. Chen, J. M. Liu, and T. B. Simpson, "Response characteristics of direct current modulation on a bandwidth-enhanced semiconductor laser under strong injection," *Opt. Commun.*, vol. 173, pp. 349–355, Jan. 2000.

[16] A. Murakami, K. Kawashima, and K. Atsuki, "Cavity resonance shift and bandwidth enhancement in semiconductor lasers with strong light injection," *IEEE J. Quantum Electron.*, vol. 39, no. 10, pp. 1196–1204, Oct. 2003.
[17] R. Lang, "Injection locking properties of a semiconductor laser," *IEEE J. Quantum Electron.*, vol. 18, no. 6, pp. 976–983, Jun. 1982.
[18] E. Doedel, A. Champneys, T. Fairgrieve, Y. Kuznetsov, B. Sandstede, and X. Wang, AUTO 2000: Continuation and bifurcation software for ordinary differential equations. [Online]. Available: http://sourceforge.net/projects/auto2000/
[19] B. Krauskopf and D. Lenstra, Eds., "Fundamental issues of nonlinear laser dynamics," in *Proc. AIP Conf.*, 2000, vol. 548.
[20] S. Wieczorek, B. Krauskopf, T. B. Simpson, and D. Lenstra, "The dynamical complexity of optically injected semiconductor lasers," *Phys. Rep.*, vol. 416, pp. 1–128, 2005.
[21] C. H. Henry, "Theory of the linewidth of semiconductor laser," *IEEE J. Quantum Electron.*, vol. 18, no. 2, pp. 259–264, Feb. 1982.
[22] M. B. Spencer and W. E. Lamb, Jr., "Laser with a transmitting window," *Phys. Rev. A*, vol. 5, pp. 884–892, 1972.
[23] S. Eriksson and Å. M. Lindberg, "Observations on the dynamics of semiconductor lasers subjected to external optical injection," *J. Opt. B: Quantum Semiclass. Opt.*, vol. 4, pp. 149–154, Apr. 2002.
[24] R. Adler, "A study of locking phenomena in oscillators," in *Proc. IRE*, 1946, vol. 34, pp. 351–357.
[25] S. Wieczorek, T. B. Simpson, B. Krauskopf, and D. Lenstra, "Global quantitative predictions of complex laser dynamics," *Phys. Rev. E*, vol. 65, pp. 045 207(R)/1–045 207(R)/4, Apr. 2002.
[26] S. Wieczorek, B. Krauskopf, and D. Lenstra, "A unifying view of bifurcations in a semiconductor laser subject to optical injection," *Opt. Commun.*, vol. 172, pp. 279–295, Dec. 1999.
[27] B. Krauskopf and S. Wieczorek, "Accumulating regions of winding periodic orbits in optically driven lasers," *Physica D*, vol. 173, pp. 114–129, Dec. 2002.
[28] A. Ritter and H. Haugh, "Theory of laser diodes with weak optical feedback I: Small signal analysis and side-mode spectra," *J. Opt. Soc. Amer. B*, vol. 10, pp. 130–144, Jan. 1993.
[29] S. Wieczorek, B. Krauskopf, T. B. Simpson, and D. Lenstra, "The dynamical complexity of optically injected semiconductor lasers," *Phys. Rep.*, vol. 416, pp. 1–128, Sept. 2005.
[30] M. Sargent, III, M. O. Scully, and W. E. Lamb, Jr., *Laser Physics*. Reading, MA: Addison-Wesley, 1974.
[31] R. Olshansky, P. Hill, V. Lanzisera, and W. Powazinik, "Frequency response of 1.3 μm InGaAsP high speed modulation lasers," *IEEE J. Quantum Electron.*, vol. QE-23, no. 9, pp. 1410–1418, Sep. 1987.
[32] Y. A. Kuznetsov, *Elements of Applied Bifurcation Theory*. New York: Springer-Verlag, 1995.
[33] T. B. Simpson, "Phase-locked microwave frequency modulations in optically-injected semiconductor lasers," *Opt. Commun.*, vol. 170, pp. 93–98, Oct. 1999.
[34] M. Nizette, T. Erneux, A. Gavrielides, and V. Kovanis, "Stability and bifurcations of periodically modulated, optically injected laser diodes," *Phys. Rev. E*, vol. 63, pp. 026 212/1–026 212/9 , Feb. 2001.
[35] H. Halbritter, R. Shau, F. Riemenschneider, B. Kogel, M. Ortsiefer, J. Rosskopf, G. Bohm, M. Maute, M. C. Amann, and P. Meissner, "Chirp and linewidth enhancement factor of 1.55 μm VCSEL with buried tunnel junction," *Electron. Lett.*, vol. 40, pp. 1266–1268, Sept. 2004.

Sebastian Wieczorek received the M.S. degree in theoretical physics from Adam Mickiewicz University, Poznań, Poland, in 1998, and the Ph.D. degree in mathematical physics from Vrije Universiteit, Amsterdam, The Netherlands, in 2002.

Currently, he is a Postdoctoral Researcher at Sandia National Laboratories, Albuquerque, NM. In June 2006, he will become a Faculty Member in the Department of Engineering, Computer Science, and Mathematics, University of Exeter, Exeter, U.K. His research interests are in the areas of applied bifurcation theory and nonlinear dynamics of (semiconductor) laser systems, such as excitation-modulated lasers, coupled lasers, lasers with optical injection, lasers with external optical feedback, lasers without population inversion, and photonic crystal lasers.

Weng W. Chow received the Ph.D. degree in physics from the University of Arizona, Tucson. His dissertation work involved fluctuation phenomena in quantum optics.

He was an Associate Professor of Physics and Astronomy at the University of New Mexico, Albuquerque, before joining Sandia National Laboratories, Albuquerque, NM, where he is a Distinguished Member of the Technical Staff. His primary research interest is in the application of microscopic theory to semiconductor laser device development. Some of this work is described in two texts: *Semiconductor-Laser Physics* and *Semiconductor-Laser Fundamentals: Physics of the Gain Materials*. His other interests include laser gyros, phased arrays, coupled lasers, quantum optics, and optical ignition of pyrotechnics.

Dr. Chow is an Adjoint Professor of Optical Sciences at the University of Arizona and an Honorary Professor of Physics at Cardiff University, Cardiff, U.K. He is currently serving on the CLEO Semiconductor Laser Program Committee and is an Associate Editor of the IEEE JOURNAL OF QUANTUM ELECTRONICS. He is a Fellow of the Optical Society of America, and a recipient of the Department of Energy, Basic Energy Science/Material Science Award and the Alexander von Humboldt Forschungspreis.

Lukas Chrostowski (M'98) was born in Warsaw, Poland, in 1975. He received the B.Eng. degree in electrical engineering from McGill University, Montreal, QC, Canada, in 1998, and the Ph.D. degree in electrical engineering and computer science from the University of California, Berkeley, in 2004.

Since January 2005, he has been an Assistant Professor in the Electrical and Computer Engineering Department at the University of British Columbia, Canada. His research interests are in the area of optoelectronics, and include injection locking of vertical-cavity surface-emitting lasers (VCSEL) for high speed analog and digital modulation, VCSEL fabrication, characterization, design and modeling, and optical communication systems.

Connie J. Chang-Hasnain (M'88–SM'92–F'98) received the B.S. degree from the University of California, Davis, in 1982, and the M.S. and Ph.D. degrees from the University of California, Berkeley, in 1984, and 1987, respectively, all in electrical engineering.

She was a Member of the Technical Staff at Bellcore from 1987 to 1992. From April 1992 to December 1995, she was an Associate Professor of electrical engineering at Stanford University, Stanford, CA. Since January 1996, she has been a Professor in the Department of Electrical Engineering, University of California, Berkeley. Since 2004, she is Director of Center for Optoelectronic Nanostructured Semiconductor Technologies (CONSRT). Her research interests are in nanostructured materials, nano- and micro-optoelectronic devices, and their applications. She coauthored 283 research papers in technical journals and conferences, and six book chapters. She also has 26 patents granted.

Prof. Chang-Hasnain was named a Presidential Faculty Fellow, a National Young Investigator, a Packard Fellow, a Sloan Research Fellow, and Outstanding Young Electrical Engineer of the Year by Eta Kappa Nu. She received the 1994 IEEE LEOS Distinguished Lecturer Award, the 2000 Curtis W. McGraw Research Award from the American Society of Engineering Education 2003 IEEE William Streifer Scientific Achievement Award, and the 2005 Gilbreth Lecturer Award from National Academy of Engineering. She is a Fellow of the OSA and IEE, and an Associate Editor for the IEEE JOURNAL OF LIGHTWAVE TECHNOLOGY. She was elected an Honorary Member of the A.F. Ioffe Institute in 2005.

Self-Induced Chaos in a Single-Mode Inversionless Laser

Sebastian Wieczorek and Weng W. Chow
Sandia National Laboratories, Albuquerque, New Mexico 87185-1086, USA
(Received 4 April 2006; published 14 September 2006)

A single-mode inversionless laser with a three-level phaseonium as an active medium can by itself exhibit complex nonlinear dynamics. Nonlinear interaction between two spectrally separated gain regions of the phaseonium and a lasing field gives rise to instabilities and chaotic self-pulsations of a type not observed in conventional lasers with population-inverted gain media. We calculate the bifurcation diagram and uncover multistability and a torus-doubling cascade in transition to chaos.

DOI: 10.1103/PhysRevLett.97.113903 PACS numbers: 42.60.Mi, 05.45.−a, 42.50.Gy, 42.55.−f

Nonlinear dynamics of lasers has been intensively studied since the laser invention in 1960. These studies provided invaluable insight into the nonlinear light-matter interaction in a cavity and uncovered phenomena including chaos, competition, excitability, and synchronization, found across different fields of science and engineering [1,2]. In particular, chaotic laser behavior motivated new technological applications such as secure chaotic communication and chaotic radars. Until 1989, the general belief was that lasers require population inversion.

During the last two decades, much attention has been devoted to the effects of atomic coherence and interference in a coherently prepared multilevel medium called phaseonium [3]. For the example from Fig. 1, it was found that phase coherence, or quantum coherence, created between two levels with a dipole-forbidden transition ($b \leftrightarrow c$) may cause unusual optical properties of the dipole-allowed transitions ($a \leftrightarrow b$) such as ultrahigh refractive index, vanishing absorption, and gain without population inversion. These discoveries led to phaseonium based lasers, called phasers [3], that do not require population inversion [4–8]. Owing to the nature of the active medium, phasers have nonlinearities that are very different from those found in conventional (population-inverted) lasers, and the resulting instabilities are not well understood. A further understanding of the phasers' nonlinear behavior, in particular, their differences from conventional lasers, is important from a fundamental viewpoint. The stability of various types of phaser output including continuous wave (cw), periodic, quasiperiodic, and chaotic lasing without inversion (LWI), as well as the possibility to control them, is becoming of great practical interest.

A single-mode three-level phaser is a paradigm of LWI [9] and the first step in understanding nonlinear dynamics of more complicated multimode phasers [10]. Although phasers show more potential for richer dynamics than conventional lasers, nonlinear dynamics analyses of LWI in single-mode, three-level phasers revealed only bistability and periodic self-pulsations [11–13]. These behaviors are much simpler than the Lorentz-type chaos reported in single-mode two- and three-level conventional lasers [1,14,15]. In particular, no chaotic LWI has yet been reported in single-mode, three-level phasers.

This Letter shows theoretically that a single-mode, three-level phaser can exhibit further instabilities and chaos of the type different than reported to date with lasers and phasers. We calculated the bifurcation diagram of a single-mode, three-level phaser and uncovered special codimension-two [16] bifurcation points that are sources of periodic, quasiperiodic, and chaotic LWI, as well as multistability. Most interesting is the self-induced torus-doubling cascade to chaotic LWI, a novel dynamical phenomenon which is not yet fully understood. It has been observed in numerical studies of dissipative media, coupled electronic circuits, forced climate model, and Navier-Stokes flow, as well as in experiments involving electrochemical reactions, arrays of convective oscillators, and ferroelectric crystals near phase transition [17]. A phaser is the first reported example of an optical system that shows a self-induced torus-doubling cascade and may contribute to a better understanding of this general phenomenon.

The results are obtained from solving the Maxwell-Bloch equations in the rotating wave approximation for a single-mode, three-level, ring-cavity phaser with the cavity resonant frequency ν_{cav} and decay rate γ_{cav}:

$$\dot{\Omega}_l = -\frac{\gamma_{\mathrm{cav}}}{2}\Omega_l - g\mathrm{Im}(\sigma_{ab}), \tag{1}$$

$$\dot{\rho}_{aa} = R_a - \frac{i}{2}[\Omega_l(\sigma_{ab} - \sigma_{ab}^*) + \Omega_p(\sigma_{ac} - \sigma_{ac}^*)], \tag{2}$$

$$\dot{\rho}_{bb} = R_b + \frac{i}{2}\Omega_l(\sigma_{ab} - \sigma_{ab}^*), \tag{3}$$

$$\dot{\sigma}_{ab} = -(\gamma_1 + i\Delta_l)\sigma_{ab} - \frac{i}{2}[\Omega_l(\rho_{aa} - \rho_{bb}) - \Omega_p\sigma_{cb}], \tag{4}$$

$$\dot{\sigma}_{ac} = -(\gamma_2 + i\Delta_p)\sigma_{ac} - \frac{i}{2}[\Omega_p(\rho_{aa} - \rho_{cc}) - \Omega_l\sigma_{cb}^*], \tag{5}$$

$$\dot{\sigma}_{cb} = -[\gamma_3 + i(\Delta_l - \Delta_p)]\sigma_{cb} - \frac{i}{2}(\Omega_l\sigma_{ac}^* - \Omega_p\sigma_{ab}). \tag{6}$$

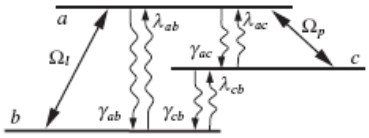

FIG. 1. A three-level scheme for inversionless gain.

The Rabi frequencies are defined as $\Omega_l(t) = \mu_{ab}E_l(t)/\hbar$ and $\Omega_p = \mu_{ac}E_p/\hbar$, where the slowly varying $E_l(t)$ and constant E_p are the real amplitudes of the lasing and coherent-pump electric fields, respectively, and μ_{ab} and μ_{ac} are the dipole moments. The gain coefficient is defined as $g = N|\mu_{ab}|^2\nu_l\Gamma/(\hbar\epsilon)$, where N is the atomic density, ν_l is the lasing-field frequency, and Γ is the optical-mode confinement factor. We assumed a time-independent pump-field phase, and the time derivative of the slowly varying lasing-field phase $\dot{\phi}_l = -g\mathrm{Re}(\sigma_{ab})/\Omega_l$ enters into $\Delta_l = \Delta_{\mathrm{cav}} - \dot{\phi}_l$, where the cavity detuning is defined as $\Delta_{\mathrm{cav}} = \nu_{ab} - \nu_{\mathrm{cav}}$. $\Delta_p = \nu_{ac} - \nu_p$, where ν_{ij} is the atomic frequency of the $i \leftrightarrow j$ transition and ν_p is the coherent-pump-field frequency. ρ_{ii} is the population of level i, and we assumed $\rho_{aa} + \rho_{bb} + \rho_{cc} = 1$. $R_a = -(\gamma_{ab} + \gamma_{ac} + \lambda_{ac})\rho_{aa} + (\lambda_{ab} - \lambda_{ac})\rho_{bb} + \lambda_{ac}$ and $R_b = (\gamma_{ab} - \gamma_{cb})\rho_{aa} - (\gamma_{cb} + \lambda_{ab} + \lambda_{cb})\rho_{bb} + \gamma_{cb}$ describe incoherent pump and decay processes, where γ_{ij} is the decay rate from i to j, and λ_{ij} is the pump rate from j to i, as indicated in Fig. 1. σ_{ij} are the slowly varying complex amplitudes of the off-diagonal elements of density matrix $\{\rho_{ij}\}$, and $\gamma_1 = (\gamma_{ab} + \gamma_{ac} + \lambda_{ab} + \lambda_{cb})/2$, $\gamma_2 = (\gamma_{ab} + \gamma_{ac} + \gamma_{cb} + \lambda_{ac})/2$, and $\gamma_3 = (\gamma_{cb} + \lambda_{ab} + \lambda_{ac} + \lambda_{cb})/2$ are the corresponding dephasing rates [12].

The stable fixed point of Eqs. (1)–(6) with $\Omega_l = 0$ corresponds to a phaser below threshold (off), and a stable fixed point with $\Omega_l > 0$ corresponds to cw LWI. Periodic orbit corresponds to LWI with periodically self-pulsating intensity (sp). As the parameters are changed, the solutions of Eqs. (1)–(6) can change as well. Qualitative changes in the system's dynamics, i.e., the bifurcations [16], are calculated with the bifurcation continuation package AUTO [18]. Transition from below threshold to cw LWI occurs typically via supercritical pitchfork bifurcation. In supercritical Hopf bifurcation, the stable point becomes unstable by giving rise to stable periodic orbit. In subcritical Hopf bifurcation, the unstable point may become stable by giving rise to unstable periodic orbit. A pair of stable and unstable periodic orbits may disappear in the saddle node of limit cycle bifurcation.

Bifurcations of Eqs. (1)–(6) are calculated in the $(\Omega_p, \Delta_{\mathrm{cav}})$ plane for $\Delta_p = 0$, $\gamma_{\mathrm{cav}} = 0.03\gamma$, $\gamma_{ab} = 0.055\gamma$, $\gamma_{ac} = 0$, $\gamma_{cb} = 0.0055\gamma$, $\lambda_{ab} = 0.045\gamma$, $\lambda_{ac} = 0.45\gamma$, and $\lambda_{cb} = 0$. In the absence of the lasing and coherent-pump field we have $\rho^0_{aa} = 0.45$, $\rho^0_{bb} = 0.55$, and $\rho^0_{cc} = 0$. Parameters are scaled with respect to a free parameter γ, and g is given in the figure captions. Chaos is found for $g/\gamma^2 = 100$. Choosing $\gamma = 4 \times 10^8\ \mathrm{s}^{-1}$, using the definition of g and assuming 1 D for μ_{ij}, 10 μm laser wavelength, and $\Gamma = 10^{-4}$, the required atomic density for observing chaos is $N = 4.5 \times 10^{23}\ \mathrm{m}^{-3}$. For room temperature, this corresponds to an active medium gas pressure of 1842 Pa or 13.9 Torr. The dephasing rates, $\gamma_i \sim 10^8\ \mathrm{s}^{-1}$, and the population decay rates, $\gamma_{ij} \sim 10^6\ \mathrm{s}^{-1}$, are consistent with the values found in molecular gases. Furthermore, $\Omega/\gamma = 1$ means a drive field intensity of 21 W/cm^2, and $\gamma_{\mathrm{cav}} = 1.2 \times 10^7\ \mathrm{s}^{-1}$.

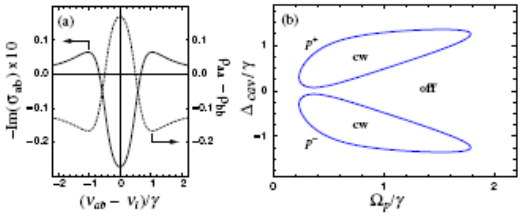

FIG. 2 (color online). (a) Gain (solid curve) and population difference (dashed curve) for the three-level phaseonium from Fig. 1 without a cavity; calculated with Eqs. (2)–(6) for $\Omega_l/\gamma = 0.5$ and $\Omega_p/\gamma = 1$. (b) Bifurcation diagram of LWI for the three-level phaseonium inside a ring-cavity; calculated with Eqs. (1)–(6) for $g/\gamma^2 = 1$. Regions of LWI are bounded by the p curves; cw marks continuous wave LWI and off is for laser below threshold. The laser is operated near its lasing threshold.

The phaseonium gain per unit length for the $a \leftrightarrow b$ transition is related to the slowly varying polarization σ_{ab} according to gain $= -g\sqrt{\epsilon_r}\mathrm{Im}(\sigma_{ab})/(c\Gamma\Omega_l)$. Figure 2(a) shows the gain profile (solid curve) and population inversion (dashed curve) assuming no cavity and a weak cw probe Ω_l. For incoherent pump and decay rates such that $\rho^0_{cc} - \rho^0_{aa} < 0$, quantum coherence σ_{cb} induces two spectrally separated inversionless-gain regions [9,12]. An interesting question arises as to what happens when this phaseonium is placed inside a cavity.

Figure 2(b) depicts the bifurcation diagram in the $(\Delta_{\mathrm{cav}}, \Omega_p)$ plane in the close vicinity of the lasing threshold. The cw LWI occurs detuned from the atomic resonance inside two islands bounded by the pitchfork bifurcation curves p^+ and p^-. The diagram from Fig. 2(b) may change drastically if the laser is operated further above threshold. In particular, as g increases, the two LWI regions from Fig. 2(b) grow in size and interact in a very nonlinear fashion. The previous studies focused on lasing near threshold. They reported bistability and periodic self-pulsations around zero cavity detuning where the two LWI regions overlap slightly [11–13]. This Letter uncovers further and more complicated LWI instabilities characteristic for inversionless lasing far above threshold.

Figure 3 shows the bifurcation diagrams in the $(\Delta_{\mathrm{cav}}, \Omega_p)$ plane that are typical for LWI far above threshold. The two LWI regions overlap significantly, and for $g/\gamma^2 \gtrsim 7$, there are four intersection points between p^+

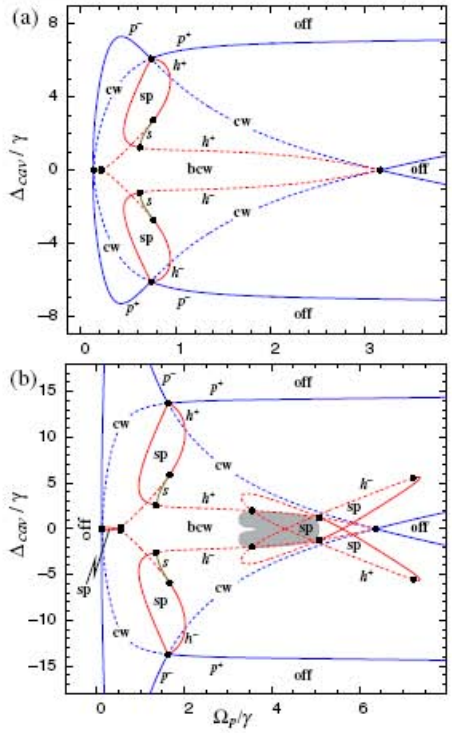

FIG. 3 (color online). Bifurcation diagram of LWI for (a) $g/\gamma^2 = 25$ and (b) $g/\gamma^2 = 100$. Region of LWI is bounded by the solid parts of the p curves; cw marks continuous wave LWI, bcw marks bistable continuous wave LWI, unshaded sp marks periodic self-pulsing LWI, shaded sp roughly marks nonperiodic self-pulsing LWI, and off is for laser below threshold. The laser is operated far above its lasing threshold.

and p^-, called codimension-two double-pitchfork bifurcations. At each point, (i) p^+ and p^- change from supercritical (solid curves) to subcritical (dashed curves) and (ii) Hopf bifurcation curves h appear, giving rise to regions of periodic self-pulsations (solid parts of h) and bistable cw LWI (dashed parts of h). Also, there are saddle node of limit cycle bifurcations s which partially bound regions of periodic self-pulsations. In contrast to Fig. 2(b), the diagram in Fig. 3(a) has a region of bistability at the atomic resonance and three regions of periodic self-pulsations: two located off the atomic resonance and a significantly smaller one at the origin of the (Δ_{cav}, Ω_p) plane [more distinct in Fig. 3(b)].

Upon further increasing g, two additional Hopf bifurcation curves h^+ and h^- appear, giving rise to additional regions of self-pulsations [Fig. 3(b)]. Most importantly, there are now four intersection points between different $h^{+(-)}$ curves, called codimension-two double-Hopf bifurcations. Out of 11 possible cases of a double-Hopf bifurcation [16] we encountered the most complicated one, which involves quasiperiodic and chaotic self-pulsations indicated roughly by the shaded region in Fig. 3(b). Here, we present two highlights of complicated LWI: torus doubling to chaos and multistability.

The torus-doubling cascade shows some similarities to the well-known infinite period-doubling cascade [19] but differs in at least two significant aspects. First, torus doubling requires at least a four-dimensional vector field. Second, a torus-doubling cascade involves an interplay between two types of transition to chaos, namely, period doubling and the breakup of tori. In fact, the tori break up within certain parameter intervals around each doubling point. These intervals eventually overlap, owing to the accumulation of subsequent doubling points, and this effect truncates the doubling cascade. If the two frequencies of the torus f_1 and f_2 are comparable, one expects long intervals with broken-up tori and only a few doubling steps. If $f_1 \gg f_2$, as is in our case, one expects short intervals with broken-up tori (possibly below what can be detected numerically) and many more torus-doubling steps [20]. In Fig. 4, the torus-doubling cascade is illustrated with (top row) attractors in the Poincaré section and (bottom row) corresponding power spectra of the phaser field

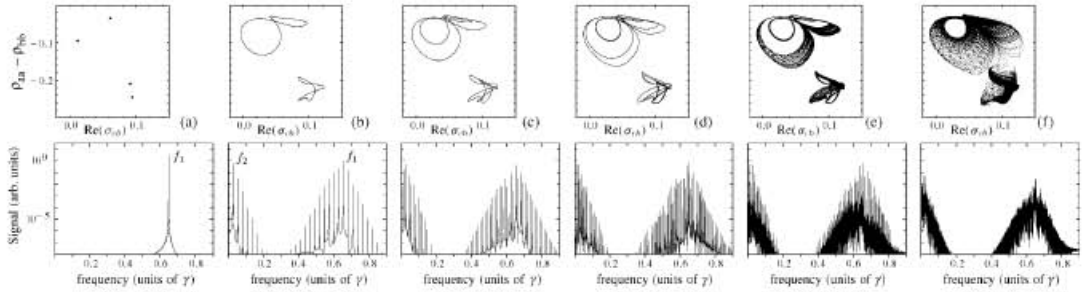

FIG. 4. Torus doubling in transition to chaotic LWI shown as (top row) attractors in the projection of the Poincaré section $\{\mathrm{Im}(\sigma_{ab}) = 0\}$ and (bottom row) power spectra of $\Omega_i(t)^2$. $g/\gamma^2 = 100$, $\Omega_p/\gamma = 4.4$, and from (a) to (f) $\Delta_{cav}/\gamma = 1.0$, 0.3, 0.2, 0.14, 0.13, and 0.1.

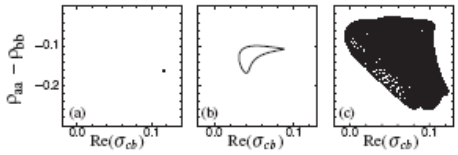

FIG. 5. Multistability between (a) stationary point, (b) periodic orbit, and (c) doubled torus for $g/\gamma^2 = 100$, $\Omega_p/\gamma = 4.4$, and $\Delta_{cav}/\gamma = 0.2$.

intensity. Figure 4(a) shows periodic orbit of frequency f_1, born in the saddle node of limit cycle bifurcation inside the shaded region in Fig. 3(b). This orbit crosses the Poincaré section 4 times. With decreasing Δ_{cav}, this periodic orbit becomes unstable via torus bifurcation and gives rise to a stable torus shown in the Poincaré section as two invariant circles [Fig. 4(b)]. Motion on the two-dimensional torus from Fig. 4(b) represents self-pulsating LWI with two frequencies, f_1 and f_2. The trajectory appears to completely fill the two circles in the Poincaré section indicating that these two frequencies are incommensurate, and the phaser output is quasiperiodic. The power spectrum has peaks at all integer linear combinations of f_1 and f_2. In torus doubling, a two-dimensional torus becomes unstable and a stable doubled torus appears [Fig. 4(c)]. This is accompanied by the appearance of additional peaks in the spectrum which can be expressed by integer linear combinations of $f_1/2$ and $f_2/2$. We were able to distinguish four consecutive torus doublings before chaotic attractor emerged with a spectrum that is a mixture of a continuous background and strong discrete peaks [Fig. 4(e)]. With further decrease in Δ_{cav}, we observed a transition to full-blown chaos with hardly any discrete peaks in the spectrum [Fig. 4(f)]. Another interesting phenomenon found inside the shaded region of Fig. 3(b) is multistability. An example involving fixed point, periodic orbit, and the doubled torus from Fig. 4(c) is shown in Fig. 5. The torus-doubling cascade can be reached by following the stable stationary point until it destabilizes along the dashed part of h^-.

In conclusion, this Letter investigates self-induced nonlinear behavior of a single-mode, three-level phaser. We considered conditions under which quantum coherence induces inversionless gain at two spectrally separated regions off the atomic resonance. Such a gain profile gives rise to two inversionless-lasing solutions. In the vicinity of the lasing threshold, each of the two solutions exist inside a separate region of inversionless lasing in the plane of the coherent-pump strength and cavity detuning. However, as the laser operates further above threshold, the two regions of inversionless-lasing overlap, giving rise to strong optical nonlinearities. These nonlinearities, governed by the processes of self- and cross saturation between the two lasing solutions [12], lead to special codimension-two double-pitchfork and double-Hopf bifurcations in the bifurcation diagram. The more interesting double-Hopf bifurcations are sources of multistability and complicated inversionless self-pulsations of the type distinctively different from instabilities found in conventional lasers. In particular, we uncovered the torus-doubling cascade in transition to chaotic lasing without inversion. A phaser is the first reported example of an optical system that shows this interesting bifurcation scenario. Note that single-mode conventional lasers have a single spectral gain region, single lasing solution, and cannot exhibit instabilities arising from the nonlinear interaction between different lasing solutions induced by quantum coherence.

This work is supported in part by the U.S. Department of Energy under Contract No. DE-AC04-94AL8500 and the Alexander von Humboldt Foundation.

[1] C. O. Weiss and R. Vilaseca, *Dynamics of Lasers* (VCH Verlagsgesellschaft, Weinheim, Germany, 1991).
[2] *Fundamental Issues of Nonlinear Laser Dynamics: Concepts, Mathematics, Physics, and Applications International Spring School*, edited by B. Krauskopf and D. Lenstra, AIP Conf. Proc. No. 548 (AIP, New York, 2000).
[3] M. O. Scully, Phys. Rep. **219**, 191 (1992).
[4] S. E. Harris, Phys. Rev. Lett. **62**, 1033 (1989).
[5] M. O. Scully, S. Y. Zhu, and A. Gavrielides, Phys. Rev. Lett. **62**, 2813 (1989).
[6] O. Kocharovskaya, Phys. Rep. **219**, 175 (1992).
[7] J. Mompart and R. Corbalán, J. Opt. B **2**, R7 (2000).
[8] A. S. Zibrov *et al.*, Phys. Rev. Lett. **75**, 1499 (1995).
[9] P. Mandel and O. Kocharovskaya, Phys. Rev. A **46**, 2700 (1992).
[10] Y. V. Radeonychev *et al.*, J. Opt. B **1**, 580 (1999).
[11] V. J. Sánchez-Morcillo, E. Roldán, and G. J. de Valcárel, Quantum Semiclass. Opt. **7**, 889 (1995).
[12] A. G. Vladimirov *et al.*, Phys. Rev. E **57**, 1499 (1998).
[13] J. Mompart, C. Peters, and R. Corbalán, Phys. Rev. A **57**, 2163 (1998).
[14] H. Haken, Phys. Lett. **53A**, 77 (1975).
[15] J. V. Moloney, J. S. Uppal, and R. G. Harrison, Phys. Rev. Lett. **59**, 2868 (1987).
[16] Yu. A. Kuznetsov, *Elements of Applied Bifurcation Theory* (Springer, New York 1995).
[17] H. W. Broer, C. Simó, and R. Vitolo, Nonlinearity **15**, 1205 (2002); J. I. Kim, H. K. Park, and H. T. Moon, Phys. Rev. E **55**, 3948 (1997); L. van Veen, Physica (Amsterdam) **210D**, 249 (2005); J. M. Flesselles, V. Croquette, and S. Jucquois, Phys. Rev. Lett. **72**, 2871 (1994); J. C. Shin and S. I. Kwun, Phys. Rev. Lett. **82**, 1851 (1999).
[18] E. Doedel *et al.*, computer code AUTO, http://sourceforge.net/projects/auto2000.
[19] A. Arnéodo, P. H. Coullet, and E. A. Spiegel, Phys. Lett. **94A**, 1 (1983).
[20] F. Schidler, H. M. Osinga, and W. Vogt, SIAM J. Appl. Dyn. Syst. **4**, 459 (2005).

40 GHz Bandwidth and 64 GHz Resonance Frequency in Injection-Locked 1.55 μm VCSELs

Lukas Chrostowski, *Member, IEEE,* Behnam Faraji, *Student Member, IEEE,* Werner Hofmann, *Student Member, IEEE,* Markus-Christian Amann, *Senior-Member, IEEE,* Sebastian Wieczorek, Weng W. Chow

***Abstract*— Injection locking is shown to greatly enhance the resonance frequency of 1.55 μm VCSELs, from 10 GHz to 60 GHz, under ultra-high injection locking conditions. Using injection locking to increase the laser resonance frequency, together with a low parasitic VCSEL design, 3-dB bandwidth of over 40 GHz was attained, a record broad-band performance for directly modulated VCSELs. VCSELs with slightly detuned polarisation modes are injection-locked with controlled polarisation angles. For the first time, a dual-resonance frequency response is observed, and is explained with a two polarisation-mode injection-locked rate equation model.**

***Index Terms*— VCSELs, Optical Injection Locking, Direct Modulation, Frequency Response.**

I. Introduction

THE resonance frequency and modulation bandwidth are two important figures-of-merit for directly modulated lasers, that determine the maximum data rate in optical communication systems. Previous state of the art in high-speed VCSEL modulation includes 20 Gb/s modulation with a 990 nm VCSEL [1], an 850 nm VCSEL with a 21 GHz bandwidth [2], 10 Gb/s modulation with a 1.55 μm VCSEL [3], [4], and most recently, a 20 GHz bandwidth allowing for 25 Gb/s modulation in a 1.1 μm VCSEL [5]. Edge-emitting lasers have achieved 3 dB modulation bandwidths of up to 40 GHz [6], [7]

In order to achieve a high modulation bandwidth, a high resonance frequency is required. Early pulsed measurements demonstrated the potential for achieving a high resonance frequency in VCSELs, up to 71 GHz [8]. In practice, however, the resonance frequency is much lower due to self-heating and reduced differential gain. One method for increasing the laser resonance frequency, thereby increasing the modulation bandwidth, is the injection locking technique [9], [10]. Previously, we have demonstrated a 50 GHz resonance frequency in ultra-high injection-locked 1.55 μm VCSELs [11], revealing an intrinsic bandwidth of greater than 50 GHz. It was found that for high injection ratio, the resonance frequency increases with increasing injection ratio, with no upper bound predicted.

Manuscript received October 30, 2006. This work was supported by the Canadian Natural Sciences and Engineering Research Council.

L. Chrostowski and B. Faraji are with the Department of Electrical and Computer Engineering, University of British Columbia, V6R 1T3 Canada (604) 822-8507, lukasc@ece.ubc.ca.

W. Hofmann and M.-C. Amann are with the Walter Schottky Institut, Technische Universitat Munchen, Am Coulombwall 3, D-85748 Garching, Germany. S.Wieczorek is with the department Applied Nonlinear Mathematics, University of Exeter, UK. W. W. Chow is with Sandia National Laboratories, Albuquerque, New Mexico, USA.

Also, a recent study reports a 44 GHz bandwidth with a peak resonance frequency of 72 GHz in an injection-locked 1.55 μm DFB laser [12].

Our previous work was focused on measurements of the intrinstic laser frequency response [11]. In these experiments, the laser parasitic was determined by a signal processing technique [13], allowing for the frequency response to be de-embedded. This paper, in contrast, presents the extrinsic frequency response of the VCSEL, including all the device parasitics, and without the de-embedding in our previous reports. To the best of our knowledge, the reported bandwidth of greater than 40 GHz is the highest for a directly modulated 1.55 μm VCSEL.

This report describes the first experimental observation of dual-resonance frequency responses for polarisation angles intentionally misaligned from the fundamental lasing mode polarisation, as shown in Figure 1. This effect is explained and results are reproduced by a two polarisation-mode rate equation model.

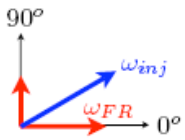

Fig. 1. Illustration of the polarisation alignment of the master laser, with respect to the two VCSEL polarisation modes. Two resonance frequencies result from the beating between the lasing mode, ω_{inj}, and the two cavity modes.

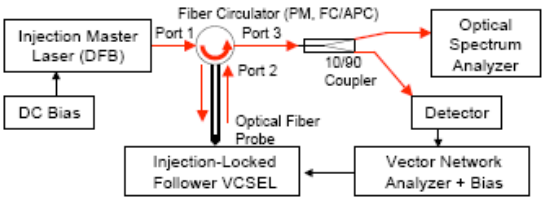

Fig. 2. Experimental setup

II. Experiments

The directly modulated VCSELs used in this experiment were 1.55 μm InGaAlAs/InP buried tunnel junction (BTJ) VCSELs [14], with a maximum laser resonance frequency

of approximately 10 GHz. The polarisation mode of the first VCSEL is at a 0.3 nm lower wavelength (or 40 GHz) than the fundamental lasing mode, as shown in Fig. 6, with a side-mode suppression ratio >40 dB.

A. Experimental Setup

The experimental setup is shown in Figure 2. The light to/from the VCSEL was coupled using an anti-reflection coated lensed polarization-maintaining (PM) fiber, aligned using a piezo-electric nano-positioning stage. The master laser is a high-power (17 dBm) Distributed Feedback (DFB) laser with a PM single mode fiber output. The light was coupled to the VCSEL via a PM circulator.

The wavelength detuning and injection power were adjusted by tuning the DFB temperature and current. The wavelength detuning is defined as $\Delta\lambda = \lambda_{DFB} - \lambda_{VCSEL}$. The injection ratio is estimated to be the free-running VCSEL power (in dBm), minus the master laser light incident on the VCSEL (in dBm). The polarisations of the DFB and VCSEL were adjusted by rotating the lensed fiber. We define the 0° polarisation to be the fundamental lasing mode, and 90° to be that of the polarisation mode. The VCSEL was probed on-wafer using a 40 GHz probe and the small signal frequency response (S21) was characterized using an Agilent E8361A 67 GHz network analyser using a resolution bandwidth of 10 Hz. The modulated VCSEL output was directly detected using a 65 GHz u2t Photonics waveguide photodiode with a known S21 response. A "thru" calibration of the network analyser was performed, to calibrate the frequency response of the cables. The frequency response of the photodetector, provided by the vendor, was subtracted from the S21 data. Thus, the frequency response data reported here is the actual response of the VCSEL, including the device parasitic. This is in contrast to previous work which included a de-embedding procedure to determine the intrinstic laser frequency response [11]. The experiments were conducted at room temperature without VCSEL temperature stabilization.

B. Experimental Results

In this study, the polarisation angle of the master laser was varied in a range of 0° (matching the fundamental VCSEL mode) to 90° (matching the polarisation mode of the VCSEL). Different frequency response behaviours were observed, as follows.

For an injection polarisation of 0°, figure 3 shows the frequency response for the laser with negative detuning values ($\Delta\lambda$) for an ultra-high injection ratio of 14.8 dB. A resonance peak up to $\sim$ 60 GHz is observed. In general, negative detuning values (in wavelength) result in sharp, undamped frequency responses, while positive detuning values result in flat responses (see ref. [11]).

At an injection polarisation of 30°, dual-resonance frequency responses were observed, as shown in Fig. 4. These frequency responses are unconventional, showing two resonance peaks rather than a single one. The corresponding optical spectra are shown in Fig. 6.

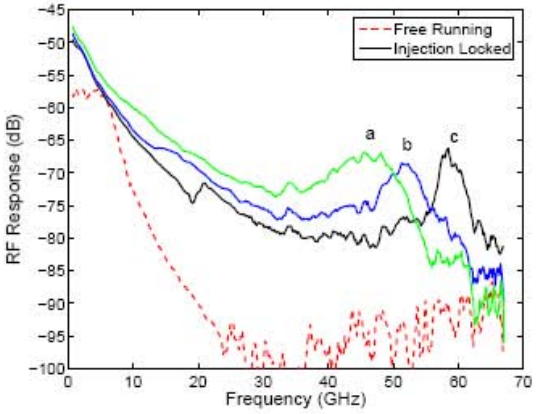

Fig. 3. Frequency response for an injection polarisation of 0°. The injection ratio was 14.8 dB, and the detuning values were a) $\Delta\lambda$ = -0.1 nm, b) -0.2 nm, c) -0.3 nm. The VCSEL bias was 1.5 mA.

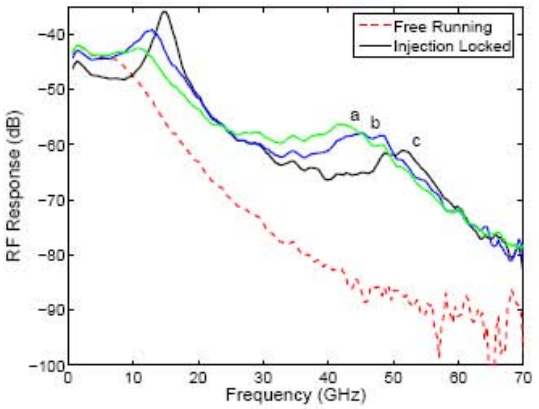

Fig. 4. Frequency response for an injection polarisation of 30°. Both polarisation modes are locked to the same master laser, leading to dual-resonance frequency responses. The injection ratio was 10 dB, and the detuning values were a) $\Delta\lambda = 0.1\ nm$, b) $0\ nm$, c) $-0.1\ nm$. The VCSEL bias was 4 mA.

Measurements for over 30 combinations of polarisation angle (varying between 10° and 60°), injection ratio (5 to 14 dB), and detuning values were conducted. The difference between the two peaks was measured, and found to be on average 36 GHz. The frequency difference measurements are summarised in Figure 5. This frequency difference approximately matches the frequency difference between the two polarisation modes in the free running laser shown in Figure 6.

For an injection polarisation of 65° to 80°, very high bandwidth ($\sim$ 40 GHz) frequency responses were observed, shown in Figure 7.

Figure 7 shows the frequency response of the injection-locked VCSEL (bias 4 mA) for several detuning conditions, under ultra-strong injection ratio. The injected optical power incident on the VCSEL was approximately 11 dBm, and the

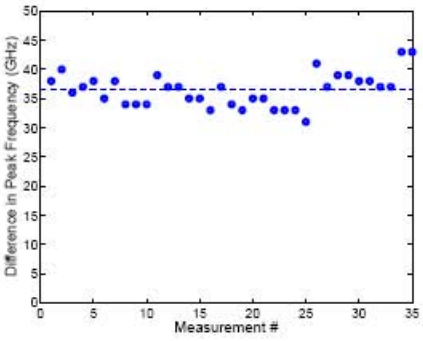

Fig. 5. An estimate of the difference between the two resonance frequencies. The values shown are the frequency separations between the two peaks in the experimental S21 responses.

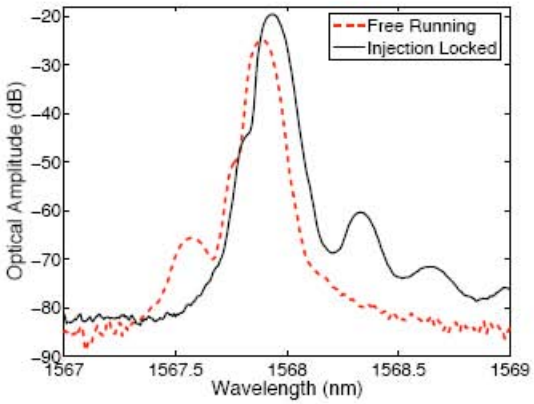

Fig. 6. Optical spectrum of the free-running laser (dotted curve) and injection-locked laser (solid). The injection-locked optical spectrum corresponds to the condition shown in Figure 4a.

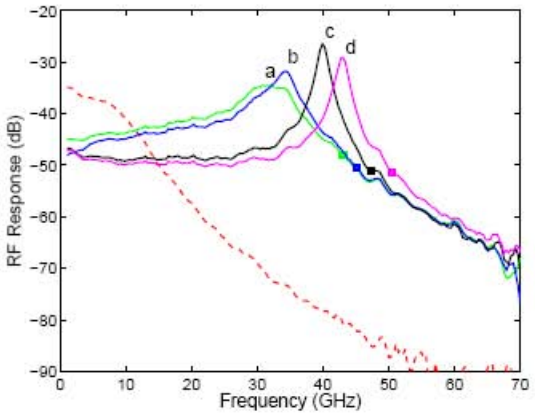

Fig. 7. Frequency response for an injection polarisation of 65 – 80°. [$\Delta\lambda$, Injection ratio, polarisation angle] = a) [+0.1 nm, 10 dB, 65°], b) [0 nm, 10 dB, 65°], c) [-0.3 nm, 10 dB, 80°], d) [-0.3 nm, 11 dB, 80°]. The VCSEL bias was 4 mA.

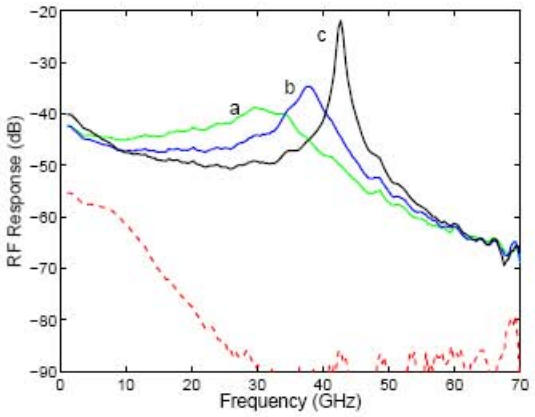

Fig. 8. Injection polarisation of 90°, locking only the 2nd polarization mode. [$\Delta\lambda$, Injection ratio] = a) [+0.1 nm, 11 dB], b) [-0.1 nm, 11 dB], c) [-0.3 nm, 11 dB].

injection ratio was 12 dB. The extrinsic bandwidth of the device was $>$ 40 GHz for the conditions shown, with the highest observed bandwidth of 49 GHz.

For an injection polarisation of 90° (orthogonal to the fundamental lasing mode), the measured frequency response is shown in Figure 8. The PM circulator used in the experiment acts as a linear polariser, thus highly attenuates the free-running frequency response, since the free-running laser emits at a 0° polarisation. The frequency response shows frequency responses similar to previous on-axis injection experiments [11], where only one resonance frequency is observed.

A second VCSEL was also studied, with a polarisation mode at a 10 GHz lower frequency. For an injection polarisation of 45°, the resulting frequency responses are shown in Figure 9, showing resonance peaks separated by $\sim$ 10 GHz.

III. Theory

A. Single-Resonance Injection Locking

In the single-resonance injection-locked VCSEL, the three relevant aspects of the modulation bandwidth experiment including 1) enhanced resonance (relaxation oscillation) frequency, 2) modulation bandwidth enhancement, and 3) enhanced modulation response at low frequencies (RF gain), can be all accurately described by the rate-equation model [15].

The significant enhancement in the resonance frequency is attributed to the beat note between the lasing mode and the shifted VCSEL cavity mode [16], [15]. Namely, the resonance frequency in strongly injected VCSELs is equal to the frequency detuning between the free-runnning and injected signals plus the shift in the cavity resonance frequency due to the injection-induced change in the active-medium

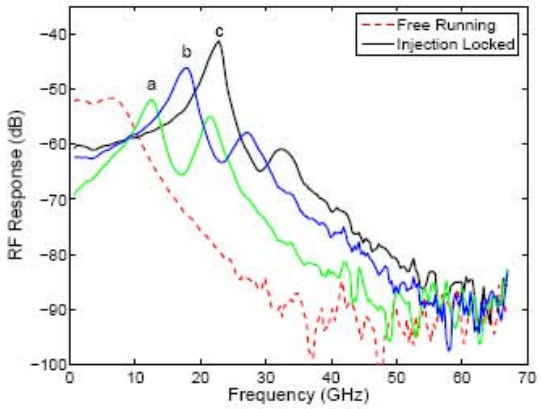

Fig. 9. Frequency response for the 2nd VCSEL with a 10 GHz polarisation mode difference, with an injection polarisation of 45°. [$\Delta\lambda$, Injection ratio] = a) [-0.04 nm, 2 dB], b) [-0.05 nm, 5 dB], c) [-0.11 nm, 6.5 dB].

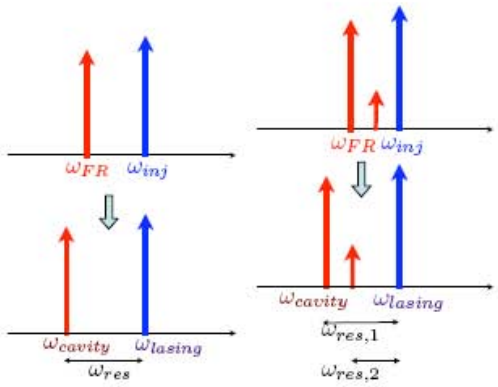

Fig. 10. a) Illustration of the cavity shift due to injection locking, leading to the injection-locked resonance frequency. ω_{FR} is the free-running optical frequency, ω_{inj} is the optical injected light frequency. When the laser is locked, its cavity frequency is shifted to ω_{cavity}, while its lasing frequency is $\omega_{lasing} = \omega_{inj}$. The new resonance frequency is $\omega_{res} = \omega_{lasing} - \omega_{cavity} = \Delta\omega_{inj} - \frac{\alpha}{2}G\Delta N$ [16]. b) Illustration of the cavity shifts experienced by both optical modes due to injection locking, leading to the injection-locked dual-resonance frequencies. $\omega_{FR1}, \omega_{FR2}$ are the free-running optical frequencies at the two polarisations $0°, 90°$, and ω_{inj} is the optical injected light frequency. When the laser is locked, the cavity frequencies are shifted to ω_{c1}, ω_{c2}, while its lasing frequency is $\omega_{lasing} = \omega_{inj}$. Thus, there are two resonance frequencies: $\omega_{res1} = \omega_{lasing} - \omega_{c1} = \Delta\omega_{inj} - \frac{\alpha}{2}G\Delta N$, $\omega_{res2} = \omega_{lasing} - \omega_{c2} = \Delta\omega_{inj} - \frac{\alpha}{2}G\Delta N - \Delta_{mode}$.

refractive index (proportional to the linewidth enhancement factor), $\omega_{res} = \omega_{lasing} - \omega_{cavity} = \Delta\omega_{inj} - \frac{\alpha}{2}G\Delta N$. This is illustrated in Figure 10a. Such enhanced resonance frequency is accompanied by the modulation bandwidth enhancement when the damping of the resonance is significantly decreased by the population pulsation and the injected VCSEL unlocks, i.e. it does not follow the current-induced variations in the injection-locked state at high modulation-frequencies [15]. This is in contrast to low modulation-frequencies where the injected VCSEL closely follows the current-induced variations in the injection-locked state [15]. Consequently, the low-frequency modulation response is determined by the slope of the light-output vs. current curve. An external optical injection can deplete the carrier density and modify the laser equilibrium such that more of the total intracavity energy is stored in the lasing field. As a result, injection-locked VCSELs can have PI curves that are much steeper than those for the free-running laser [17], leading to an increased modulation response at low frequencies.

An alternative approach based on the amplifier model has also been used to describe the effects of resonance frequency and modulation response enhancement [18]. In this model, VCSEL acts as a high-Q amplifier, amplifying the microwave modulation signals at frequencies near the resonance frequency.

Building on the previous success of the approach based on the single-mode rate-equation model, we use here the two-polarisation-mode version of the model to reproduce the double resonance frequency experiments.

B. Dual-Resonance Injection Locking

In the dual-resonance injection locking system, the two resonances are due to a beating between the lasing mode and the shifted two VCSEL polarization modes. In the VCSEL described in this experiment, the 2nd polarization mode is 40 GHz detuned from the fundamental lasing mode. Thus, the difference between the two resonances is 40 GHz. The shift for each resonance is constant for all detuning and injection ratio conditions, because the two modes share one carrier population. Thus, the shift experienced by each mode will be $\frac{\alpha}{2}G\Delta N$, and is identical for both modes. This is shown schematically in Figure 10b.

The dual-resonance effect described has been observed for polarization modes. However, the model is general in that any two (or more modes) can be locked in a similar fashion. For example, if the higher order transverse mode splitting was small enough, it could also be locked, thus leading a dual resonance response curve.

By varying the frequency difference between the fundamental and polarization mode, it is possible to design the frequency response of the injection-locked VCSEL. In particular, it may be possible to optimize for an even higher frequency laser bandwidth.

1) Rate Equation Model: Semiconductor lasers are typically described the rate equation model. This model has been applied for the case of external light interacting with the laser, including optical feedback [19] and optical injection locking [20], [21], [22]. In this work, the conventional single-mode semiconductor optical injection locking rate equation model was modified to include two optical polarisation modes.

In previous work, there have been several injection locking studies which considered multiple modes including: side-mode injection locking [23], [24]; multiple-transverse mode locking [25]; wavelength conversion [26] and polarisation switching [27]; polarisation stabilisation [28]; and 2R (reamplification and reshaping) regeneration [29]; and spin-flip effects causing quasi-stable oscillation [30].

To the best of our knowledge, this is the first work which investigates the carrier modulation properties of a two polarisation-mode injection-locked laser.

This model consists of two optical fields coupled via a common carrier density. S_1 and S_2 describe the photon density for the 0° and 90° degree polarisations, respectively, while ϕ_1 and ϕ_2 describe the corresponding optical phases for the two modes. The optical injected photon density is S_{inj}. The optical injected light is incident at a polarisation θ_P, thus the light injected into the 0° polarisation is $S_{inj} \cdot \cos(\theta_P)$, and the light injected in the 90° polarisation is $S_{inj} \cdot \sin(\theta_P)$. The 0° polarisation is assumed to be the fundamental mode (S_1, ϕ_1), with the polarisation mode detuned by a frequency Δ_{mode}.

The photon lifetime of the 2nd mode is chosen so that the side-mode suppression ratio of the free-running laser is > 35 dB, matching the experimental devices, with $\tau_{p2} = 0.9 \times \tau_{p1}$.

$$\begin{aligned}\frac{dS_1}{dt} &= \left(G - \frac{1}{\tau_p 1}\right) \cdot S_1 + R_{sp} \\ &\quad + k_c\sqrt{S_1 \cdot S_{inj}} \cdot \cos(\theta_P) \cdot \cos(\phi_1(t) - \phi_{inj}) \\ \frac{dS_2}{dt} &= \left(G - \frac{1}{\tau_p 2}\right) \cdot S_2 + R_{sp} \\ &\quad + k_c\sqrt{S_2 \cdot S_{inj}} \cdot \sin(\theta_P) \cdot \cos(\phi_2(t) - \phi_{inj})\end{aligned} \tag{1}$$

$$\begin{aligned}\frac{d\phi_1}{dt} &= \frac{\alpha}{2} G_o(N - N_{th}) - 2\pi\Delta f \\ &\quad - k_c\sqrt{\frac{S_{inj}}{S_1}} \cdot \cos(\theta_P) \cdot \sin(\phi_1(t) - \phi_{inj}) \\ \frac{d\phi_2}{dt} &= \frac{\alpha}{2} G_o(N - N_{th}) - 2\pi\Delta f + \Delta_{mode} \\ &\quad - k_c\sqrt{\frac{S_{inj}}{S_2}} \cdot \sin(\theta_P) \cdot \sin(\phi_2(t) - \phi_{inj})\end{aligned} \tag{2}$$

The carrier density is described by a single variable, N, since both optical fields interact with the same carrier population in the active region. The photon density in the carrier equation is assumed to be the sum of the two photon densities, $S_{tot} = S_1 + S_2$.

$$\frac{dN}{dt} = \frac{I}{q} - \frac{N}{\tau_s} - G \cdot S_{tot} \tag{3}$$

$$G = \frac{G_o(N - N_o)}{1 + \epsilon S_{tot}} \tag{4}$$

The parameters used for the simulations are given in Table I [15]. Significantly, these parameters correctly reproduce the modulation efficiency enhancement observed in injection-locked VCSEL experiments [15]. In particular, the carrier and photon lifetimes, as well as linewidth enhancement factor, were found to be the most important in determining to the modulation efficiency enhancement observed.

The injection-locked modes remain in orthogonal polarisations when locked, i.e. S_1 and S_2 describe the photon density for the 0° and 90° degree polarisations, even when locked. The light output from the locked laser is thus a vector addition of the two modes, and can be at a linear or elliptical polarisation, depending on the phase differences between the modes.

2) Numerical Simulations: Numerical simulations of the rate equations (1)-(4) were performed using Matlab with the ODE23 solver. First, the equations were solved for the steady-state solutions. When the two phase terms, $\phi_1(t)$ and $\phi_2(t)$, have a zero slope (with a constant phase shift between them), this indicates that they are lasing at the same wavelength; this is the "dual-locked" condition.

In the cases considered where the dual-resonance response is observed, the phase shift between the two modes is approximately a multiple of 2π. Thus, the injection-locked light output is at a linear polarisation. The angle does not necessarily match the incident light, since the photon densities of the two polarisations are not equal.

The frequency response of the system is simulated. A small signal modulation was applied to the bias current, $I = I_{bias}[1 + m\sin(2\pi f_{mod} t)]$, where m is the modulation index, I_{bias} is the bias current, and f_{mod} is the modulation frequency.

First, a simulation of injection locking at a 0° injection angle was performed, with the results shown in Figure 11. The modulation amplitude results agree with previous experiments [11]. Also shown in the figure is the microwave phase response. Just as a free-running laser exhibits a $-180°$ phase shift transition between low and high frequencies, so do single-mode injection-locked lasers [31].

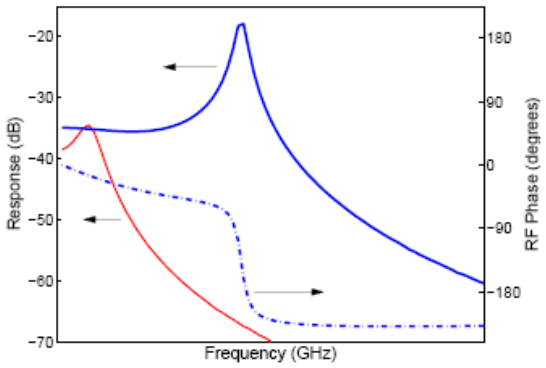

Fig. 11. Frequency response of the dual-resonance injection-locked VCSEL with light incident at a 0° polarisation, obtained by numerical simulations of the rate equations. Injection ratio = 2, Detuning = 30 GHz. Polarisation mode detuning = 35 GHz. Dotted blue curve: microwave phase, thin red curve: free-running laser S21, thick blue curve: injection-locked S21

The frequency response of each mode is individually plotted in Figure 12, shown in the dotted lines. The two responses show different resonance frequencies. These two responses are contained in each of the orthogonal polarisations. In order to determine the overall response, the vector addition of the two optical modes is performed, followed by direct detection (non-polarisation selective). This leads to the total response shown in the solid thick (blue) curve in Figure 12. For comparison, the thin solid green curve shows the scalar summation of the responses of the two modes.

Since we are performing a vector summation of the two

modes, the optical phases, as well as the electrical microwave phases must be considered in the analysis. The microwave phases of the two modes are shown in the magenta dashed-dotted curves. As can be seen, each mode experiences a $\sim -180°$ phase shift at its respective resonance frequency. The thick blue dashed-dotted curve is the microwave phase for the total response. The total response undergoes two phase change regions at each of the resonance frequencies. The total phase change from DC is $\sim -180°$, as in the case of single-mode injection-locked lasers.

Due to the microwave $-180°$ phase transitions occurring at the two different resonance frequencies, there are regions in the total frequency response where the two signals have opposite phase, thus leading to the possibility of signal cancellation. This is seen at $\sim$ 48 GHz where the signal amplitude of the two modes is similar in power but nearly opposite in phase. This effect leads to a dip in the frequency response between the two resonance peaks.

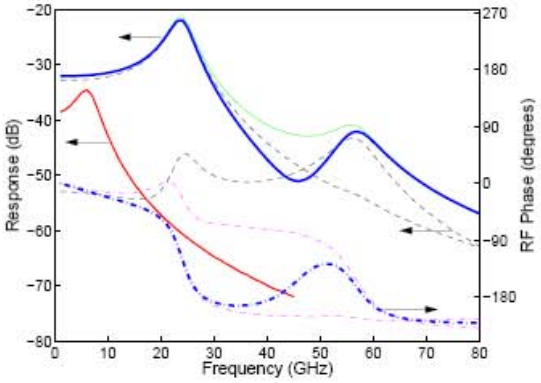

Fig. 12. Frequency response of the dual-resonance injection-locked VCSEL with light incident at a 30° polarisation, obtained by numerical simulations of the rate equations. Injection ratio = 2, Detuning = 30 GHz. Polarisation mode detuning = 35 GHz. Dotted blue curve: microwave phase, thin red curve: free-running laser S21, thick blue curve: injection-locked S21

In the simulation shown in 13, the polarisation filtering effect of the PM circulator was taken into account. The polariser is aligned with the injected light (20°), and results in a reduced contribution from the 15 GHz resonance frequency peak (owing to the 90° mode). The result is a nearly flat frequency response up to the 45 GHz resonance peak, with a 3 dB bandwidth of 54 GHz.

In this study, the polarisation mode detuning is assumed to be Δ_{mode} = 35 GHz, i.e. the polarisation mode is at a higher frequency than the fundamental mode. Simulations are also performed for the case when the 2nd mode is at lower frequency, i.e. Δ_{mode} = -35 GHz. These two cases show very similar frequency response curves, with slight differences in the amplitudes of the two peaks. The slight differences are a result of the different cavity losses for the two modes.

IV. ANALYSIS

In this study, the polarisation of the injected light was precisely controlled to determine the effects of the injected

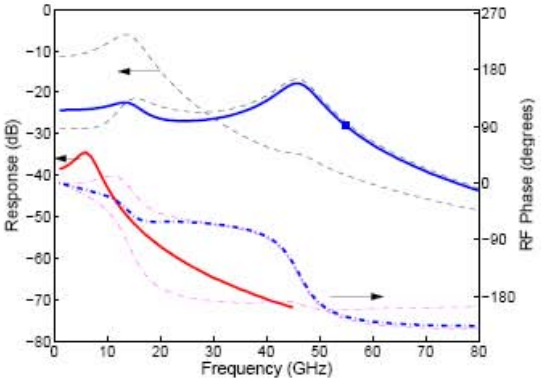

Fig. 13. Frequency response of the dual-resonance injection-locked VCSEL with light incident at a 20° polarisation, obtained by numerical simulations of the rate equations. This simulation incorporates the polarisation filtering effect of the PM circulator. The predicted 3 dB bandwidth is 54 GHz (blue square). Injection ratio = 2, Detuning = 20 GHz. Polarisation mode detuning = 35 GHz. Dotted blue curve: microwave phase, red curve: free-running laser S21, thick blue curve: injection-locked S21.

TABLE I
LIST OF SIMULATION PARAMETERS

Parameter	Symbol	Value	Units
Linewidth enhancement factor	α	5 [32]	
Bias current	I_{bias}	$4 \times I_{th}$	
Photon lifetime (mode 1)	τ_p	12.5	ps
Photon lifetime (mode 2)	τ_p	11.2	ps
Carrier lifetime	τ_s	0.2	ns
Differential gain	$\frac{dg}{dn}$	1×10^{-15}	cm^2
Cavity length	L_{cavity}	5.5	μm
Active volume	V_{active}	1.2×10^{-12}	cm^3
Injection coupling rate	k_c	802	ns^{-1}
Spontaneous emission rate	R_{sp}	127	ns^{-1}
Optical confinement factor	Γ	0.03	
Group velocity	v_g	8.8	cm/ns
Modal gain $\frac{\Gamma \frac{dg}{dn} v_g}{V_{active}}$	G_o	2.2×10^{-4}	ns^{-1}
Transparency carrier density	N_o	1.2×10^6	
Threshold carrier density	N_{th}	1.6×10^6	
Injection locking detuning	Δf	30	GHz
Injection locking power ratio	$\frac{S_{inj}}{S}$	2	

light on the polarisation modes. The VCSEL used had a polarisation mode splitting of 40 GHz, thus two resonance frequency peaks were observed in the frequency response. This was understood to be the beating between the lasing/injected light and the two cavity modes. Numerical modelling of the proposed orthogonal polarisation-mode injection locking equations were performed, demonstrating that this model predicts the experimentally observed behaviour.

With a model and physical understanding of this system, it is possible to consider engineering the frequency response of semiconductor lasers. In particular, the choice of polarisation mode splitting in buried tunnel junction (BTJ) VCSELs can be controlled by varying the degree of elipticity [33]. This would allow a nearly arbitrary choice in the resonance frequencies of the two modes: the lowest resonance frequency would be dictated primarily by the injection power ratio (and detuning),

while the second resonance peak would be present at a higher value, shifted by the polarisation mode detuning. This could allow the design of a frequency response with multiple pass-bands for microwave communication applications. Comparing to the case of a single-mode injection-locked laser with a 60 GHz resonance frequency, the injection ratio in such a case would be much smaller since the locking power would be dictated by the power required to lock nearest mode to a lower resonance frequency.

As evidenced in Figure 7, a very high extrinsic 3 dB bandwidth of >40 GHz was observed. This was also obtained in the simulations, Figure ??, where a 54 GHz bandwidth was predicted. This large bandwidth was possible in part due to the interaction of the two polarisation modes, leading to a flat frequency response at frequencies below the resonance peak. Thus, the dual-resonance system can be used to obtain a wide 3 dB bandwidth with the appropriate choice of polarisation injection angle, VCSEL polarisation mode frequency difference, and injection ratio/detuning parameters.

V. Conclusion

In this study, the injected light polarisation was precisely controlled to determine the effects of the polarisation angle on the locked frequency response. For a 0° injection (aligned with the fundamental polarisation), the frequency response of an ultra-high injection-locked VCSEL was showed resonance frequencies up to 60 GHz .

For the first time, a double-resonance frequency response was observed, for the case of a VCSEL with a polarisation mode splitting of 40 GHz, with a non-zero injection polarisation angle. This is understood to be the beating between the lasing field and the two cavity polarisation modes. Numerical modelling of the orthogonal polarisation-mode injection-locked equations were performed, demonstrating that this model reproduces the experimentally observed behaviour. Such frequency responses have the potential of finding applications in dual-band transmission systems, or for increasing the 3 dB bandwidth of directly modulated VCSELs. A >40 GHz extrinsic bandwidth was demonstrated with this approach.

Appendix
Derivation of the two-polarisation rate equations

The derivation of the two-polarisation mode equations begins with the single-mode injection locking rate equation (Eq. 52 in [26]). It is written in terms of the normalised field envelope, A, where $|A|^2 = S$ and S is the photon number, and $A_{inj} = \sqrt{S_{inj}}$ is the injected field.

$$\frac{dA}{dt} = \left\{\frac{1}{2}(1+i\alpha)G_o(N-N_{th}) - i\Delta\omega_i\right\}\cdot A + k_c A_{inj} \quad (5)$$

This can also be written as the following, since $G_o(N - N_{th}) = G_o(N - N_o) - \frac{1}{\tau_p}$, where N_o is the transparency carrier number, N_{th} is the threshold carrier number.

$$\frac{dA}{dt} = \left\{\frac{1}{2}(1+i\alpha)\left[G_o(N-N_o) - \frac{1}{\tau_p}\right] - i\Delta\omega_i\right\}\cdot A + k_c A_{inj} \quad (6)$$

We consider two polarisation mode field amplitudes, A_1 and A_2, for the 0° and 90° degree polarisations, respectively. The 0° polarisation is assumed to be the fundamental mode. The optical injected field, A_{inj}, is incident at a polarisation θ_P, thus the field injected into the 0° polarisation is $\sqrt{S_{inj1}} = A_{inj1} = A_{inj}\cdot\cos(\theta_P)$, and the field injected in the 90° polarisation is $\sqrt{S_{inj2}} = A_{inj2} = A_{inj}\cdot\sin(\theta_P)$. The polarisation modes are detuned by a frequency Δ_{mode}, i.e. $E_1 \propto A_1 e^{i(\phi_1+\omega_{FR}t)}$ is field of the 0° polarisation, while $E_2 \propto A_2 e^{i\{\phi_2+(\omega_{FR}+\Delta_{mode})t\}}$ is field of the higher-order 90° polarisation. The threshold carrier numbers for the two modes are N_{th1} and N_{th2}, with the modes having photon lifetimes τ_{p1} and τ_{p2}. The equations for the two modes are thus:

$$\begin{aligned}\frac{dA_1}{dt} &= \left[\frac{1}{2}(1+i\alpha)G_o(N-N_{th1}) - i\Delta\omega_i\right]\cdot A_1 + k_c A_{inj1}\\ \frac{dA_2}{dt} &= \left[\frac{1}{2}(1+i\alpha)G_o(N-N_{th2}) - i\Delta\omega_i + i\Delta\omega_{mode}\right]\cdot A_2 + k_c A_{inj2}\end{aligned} \quad (7)$$

These equations can be written in terms of the photon numbers and phase, for the purpose of numerical simulations. S_1 and S_2 describe the photon number for the 0° and 90° degree polarisations, respectively, while ϕ_1 and ϕ_2 describe the corresponding optical phases for the two modes. The photon number equation is found by writing:

$$\frac{dS_1}{dt} = \frac{dA_1^* A_1}{dt} = \frac{dA_1^*}{dt}A_1 + \frac{dA_1}{dt}A_1^* \quad (8)$$

$$\begin{aligned}\frac{dS_1}{dt} &= G_o(N-N_{th1})\cdot S + 2k_c\cdot A_{inj}\cos\theta_P\cdot A_1\cdot\cos(\theta_1-\theta_{inj})\\ &= G_o(N-N_{th1})\cdot S + 2k_c\sqrt{S_{inj}S_1}\cdot\cos\theta_P\cos(\theta_1-\theta_{inj})\end{aligned} \quad (9)$$

Similarly,

$$\frac{dS_2}{dt} = G_o(N-N_{th2})\cdot S + 2k_c\sqrt{S_{inj}S_2}\cdot\sin\theta_P\cos(\theta_2-\theta_{inj}) \quad (10)$$

The phase equation is found by writing:

$$\begin{aligned}\frac{dA_1}{dt} &= \frac{d|A_1|}{dt}e^{i\theta_1} + |A_1|i\frac{d\theta_1}{dt}e^{i\theta_1}\\ &= \left(\frac{1}{2}(1+i\alpha)G_o(N-N_{th}) - i\Delta\omega_i\right)\cdot A + k_c A_{inj}\\ \frac{dA_1^*}{dt} &= \frac{d|A_1^*|}{dt}e^{i\theta_1} - |A_1|i\frac{d\theta_1}{dt}e^{-i\theta_1}\\ &= \left(\frac{1}{2}(1-i\alpha)G_o(N-N_{th}) + i\Delta\omega_i\right)\cdot A^* + k_c A_{inj}^*\end{aligned} \quad (11)$$

and solving for $\frac{d\theta_1}{dt}$. This yields:

$$\begin{aligned}\frac{d\theta_1}{dt} =& \frac{\alpha}{2}G_o(N-N_{th1}) - \Delta\omega_i - k_c\frac{A_{inj1}}{A_1}\cdot\sin(\theta_1-\theta_{inj}) \\ =& \frac{\alpha}{2}G_o(N-N_{th1}) - \Delta\omega_i \\ & - k_c\sqrt{\frac{S_{inj}}{S_1}}\cdot\cos\theta_P\cdot\sin(\theta_1-\theta_{inj})\end{aligned} \tag{12}$$

Similarly,

$$\begin{aligned}\frac{d\theta_2}{dt} =& \frac{\alpha}{2}G_o(N-N_{th2}) - \Delta\omega_i + \Delta_{mode} \\ & - k_c\sqrt{\frac{S_{inj}}{S_2}}\cdot\sin\theta_P\cdot\sin(\theta_2-\theta_{inj})\end{aligned} \tag{13}$$

ACKNOWLEDGMENT

Chrostowski would like to thank M. J. Adams and X. Zhao for useful discussions. The authors thank Dr. M. Ortsiefer and J. Rosskopf at Vertilas GmbH for on-wafer testing of the laser chips.

REFERENCES

[1] D. Kucharski, Y. Kwark, D. Guckenberger, D. Kuchta, K. Kornegay, M. Tan, C. K. Lynn, and A. Tandon, "A 20 Gb/s CMOS VCSEL driver with pre-emphasis and regulated output impedance in 0.13um CMOS," *IEEE International Solid-State Circuits Conference (ISSCC)*, p. 222, 2005.

[2] K. Lear, M. Ochiai, V. Hietala, H. Hou, B. Hammons, J. Banas, and J. Nevers, "High-speed vertical cavity surface emitting lasers," *Digest of the IEEE/LEOS Summer Topical Meetings*, pp. 53–4, 1997. [Online]. Available: http://dx.doi.org/10.1109/LEOSST.1997.619101

[3] M. Ortsiefer, R. Shau, F. Mederer, R. Michalzik, J. Rosskopf, G. Bohm, F. Kohler, C. Lauer, M. Maute, and M.-C. Amann, "High-speed modulation up to 10 Gbit/s with 1.55 μm wavelength InGaAlAs VCSELs," *IEE Electronics Letters*, vol. 38, no. 20, pp. 1180–1181, 2002.

[4] W. Hofmann, N. H. Zhu, M. Ortsiefer, G. Bohm, J. Rosskopf, L. Chao, S. Zhang, M. Maute, and M. C. Amann, "10-Gb/s data transmission using BCB passivated 1.55 μm InGaAlAs-InP VCSELs," *IEEE Photon. Technol. Lett.*, vol. 18, no. 2, pp. 424–426, 2006.

[5] N. Suzuki, H. Hatakeyama, K. Fukatsu, T. Anan, K. Yashiki, and M. Tsuji, "25-Gbps operation of 1.1 μm-range InGaAs VCSELs for high-speed optical interconnections," *Optical Fiber Communication Conference*, 2006.

[6] S. Weisser, E. C. Larkins, K. Czotscher, W. Benz, J. Daleiden, I. Esquivias, J. Fleissner, J. D. Ralston, B. Romero, R. E. Sah, A. Schonfelder, and J. Rosenzweig, "Damping-limited modulation bandwidths up to 40 GHz in undoped short-cavity In0.35Ga0.65As-GaAs multiple-quantum well lasers," *IEEE Photon. Technol. Lett.*, vol. 8, no. 5, pp. 608–610, 1996.

[7] K. Nakahara, T. Tsuchiya, T. Kitatani, K. Shinoda, T. Taniguchi, T. Kikawa, M. Aoki, and M. Mukaikubo, "High extinction ratio operation at 40-Gb/s direct modulation in 1.3 μm InGaAlAs-MQW RWG DFB lasers," *Optical Fiber Communication Conference*, pp. 3 pp. –, 2006.

[8] D. Tauber, G. Wang, R. S. Geels, J. E. Bowers, and L. A. Coldren, "Large and small signal dynamics of vertical cavity surface emitting lasers," *Applied Physics Letters*, vol. 62, no. 4, pp. 325–327, 1993.

[9] J. M. Liu, H. F. Chen, X. J. Meng, and T. B. Simpson, "Modulation bandwidth, noise, and stability of a semiconductor laser subject to strong injection locking," *IEEE Photon. Technol. Lett.*, vol. 9, no. 10, pp. 1325–1327, 1997.

[10] X. J. Meng, C. Tai, and M. C. Wu, "Experimental demonstration of modulation bandwidth enhancement in distributed feedback lasers with external light injection," *IEE Electronics Letters*, vol. 34, no. 21, pp. 2031–2032, 1998.

[11] L. Chrostowski, X. Zhou, and C. J. Chang-Hasnain, "Microwave performance of optically injection-locked VCSELs," *IEEE Trans. Microwave Theory Tech.*, vol. 54, no. 2, pp. 788–796, Feb. 2006.

[12] E. Lau, H.-K. Sung, and M. Wu, "Ultra-high, 72 GHz resonance frequency and 44 GHz bandwidth of injection-locked 1.55 μm DFB lasers," *Optical Fiber Communication Conference*, pp. 3 pp. –, 2006//.

[13] L. Chrostowski, X. Zhao, and C. J. Chang-Hasnain, "Very high resonance frequency (>40 GHz) optical injection-locked 1.55 μm VCSELs," *Microwave Photonics Conference*, pp. 255–258, Oct. 2004.

[14] W. Hofmann, N. H. Zhu, M. Ortsiefer, G. Bohm, Y. Liu, and M. C. Amann, "High speed (> 11 GHz) modulation of BCB-passivated 1.55 μm InGaAlAs-InP VCSELs," *Electronics Letters*, vol. 42, no. 17, pp. 976–977, 2006.

[15] S. Wieczorek, W. Chow, L. Chrostowski, and C. J. Chang-Hasnain, "Improved semiconductor-laser dynamics from induced population pulsation," *IEEE J. Quantum Electron.*, vol. 42, no. 6, pp. 552–62, 2006. [Online]. Available: http://dx.doi.org/10.1109/JQE.2006.874753

[16] A. Murakami, K. Kawashima, and K. Atsuki, "Cavity resonance shift and bandwidth enhancement in semiconductor lasers with strong light injection," *IEEE J. Quantum Electron.*, vol. 39, no. 10, pp. 1196–1204, 2003.

[17] X. Zhao, L. Chrostowski, and C. J. Chang-Hasnain, "Extinction ratio of injection-locked vcsels," *Lasers and Electro-Optics Society Conference*, vol. 1, no. 244 – 245, Nov. 8-9 2004.

[18] X. Zhao, C. J. Chang-Hasnain, W. Hofmann, and M.-C. Amann, "Modulation efficiency enhancement of 1.55-μm injection-locked VCSELs," *IEEE International Semiconductor Laser Conference*, pp. 125–126, Sept. 2006.

[19] R. Lang and K. Kobayashi, "External optical feedback effects on semiconductor injection laser properties," *IEEE J. Quantum Electron.*, vol. 16, pp. 347–355, Mar. 1980.

[20] N. Schunk and K. Petermann, "Noise analysis of injection-locked semiconductor injection lasers," *IEEE J. Quantum Electron.*, vol. QE-22, no. 5, pp. 642–650, 1986.

[21] R. Lang, "Injection locking properties of a semiconductor laser," *IEEE J. Quantum Electron.*, vol. QE-18, no. 6, pp. 976–983, 1982.

[22] I. Petitbon, P. Gallion, G. Debarge, and C. Chabran, "Locking bandwidth and relaxation oscillations of an injection-locked semiconductor laser," *IEEE J. Quantum Electron.*, vol. 24, no. 2, pp. 148–154, 1988.

[23] J.-M. Luo and M. Osinski, "Multimode small-signal analysis of side-mode injection-locked semiconductor lasers," *Japanese Journal of Applied Physics*, vol. 31, pp. L685–L688, June 1992.

[24] Y. Hong and K. A. Shore, "Locking characteristics of a side-mode injected semiconductor laser," *IEEE J. Quantum Electron.*, vol. 35, no. 11, pp. 1713–1717, 1999.

[25] T. Fishman and A. Hardy, "Effect of spatial hole burning on injection-locked vertical-cavity surface-emitting laser arrays," *Applied Optics*, vol. 39, no. 18, pp. 3108–3114, 2000.

[26] J. Horer and E. Patzak, "Large-signal analysis of all-optical wavelength conversion using two-mode injection-locking in semiconductor lasers," *IEEE J. Quantum Electron.*, vol. 33, no. 4, pp. 596–608, 1997.

[27] Z. G. Pan, S. Jiang, M. Dagenais, R. A. Morgan, K. Kojima, M. T. Asom, R. E. Leibenguth, G. D. Guth, and M. W. Focht, "Optical injection induced polarization bistability in vertical-cavity surface-emitting lasers," *Applied Physics Letters*, vol. 63, pp. 2999–3001, Nov. 1993.

[28] S. Bandyopadhyay, Y. Hong, P. S. Spencer, and K. A. Shore, "VCSEL polarization control by optical injection," *IEEE J. Lightwave Technol.*, vol. 21, no. 10, pp. 2395–2404, 2003.

[29] Y. Onishi and F. Koyama, "All-optical regeneration using a vertical-cavity surface-emitting laser with external light injection," *IEICE Trans. Electron. (Japan)*, vol. E87-C, no. 3, pp. 409–15, Mar. 2004.

[30] A. Homayounfar and M. Adams, "Polarisation effects in optically-injected VCSELs," *IEE Electronics Letters*, vol. 42, no. 9, pp. 537–538, Apr. 2006.

[31] L. Chrostowski, "Optical injection locking of vertical cavity surface emitting lasers," Ph.D. dissertation, University of California, Berkeley, 2004.

[32] H. Halbritter, R. Shau, F. Riemenschneider, B. Kogel, M. Ortsiefer, J. Rosskopf, G. Bohm, M. Maute, M.-C. Amann, and P. Meissner, "Chirp and linewidth enhancement factor of 1.55 μm VCSEL with buried tunnel junction," *IEE Electronics Letters*, vol. 40, no. 20, pp. 1266–8, Sept. 2004.

[33] M. Ortsiefer, M. Grau, J. Rosskopf, R. Shau, K. Windhorn, E. Rönneberg, G. Bohm, W. Hofmann, O. Dier, and M.-C. Amann, "InP-based VCSELs with buried tunnel junction for optical communication and sensing in the 1.3-2.3 μm wavelength range," *IEEE International Semiconductor Laser Conference*, p. WB7, 2006.

Lukas Chrostowski (M98) was born in Warsaw, Poland, in 1975. He received the B.Eng. degree in electrical engineering from McGill University, Montreal, Canada, in 1998, and the Ph.D. degree in electrical engineering and computer science from the University of California, Berkeley in 2004. Since January 2005, he has been an Assistant Professor in the Electrical and Computer Engineering department at the University of British Columbia. His research interests are in the area of optoelectronics, and include injection locking of vertical-cavity surface emitting lasers (VCSEL) for high speed analog and digital modulation, VCSEL fabrication, characterization, design and modeling, and optical communication systems.

Behnam Faraji

Werner Hofmann was born in Erlenbach, Germany, in 1978. He received its Diploma (M. Sc.) degree in electrical engineering and IT in 2003 from the Munich University of Technology (Technische UniversitŁt Mnchen), Germany, in 2003.

During his studies focusing on optoelectronics and RF-technology he already worked at the Walter Schottky Institute developing a dry-etch process for High-Speed VCSEL manufacturing. Since 2003 he is with Prof. Amann working towards his Ph.D. degree focusing on High-Speed VCSELs. The last years he co-authored several papers on 1.55μm VCSELs and their applications.

Markus-Christian Amann received the Diplom degree in electrical engineering in 1976 and the Dr.-Ing. degree in 1981, both from the Technical University of Munich. During his thesis work he studied superluminescent diodes and low-threshold laser diodes and developed the AlGaAs-GaAs metal-clad ridge-waveguide laser. From 1981 to 1994 he was with the Corporate Research Laboratories of the Siemens AG in Munich where he was involved in the research on long-wavelength InGaAsP-InP laser diodes. In 1994 he joined the Department of Electrical Engineering at the University of Kassel as a full professor for "Technical Electronics". Since 1997 he holds the Chair of Semiconductor Technology at the Walter Schottky Institute of the Technical University of Munich, where he is currently engaged in the research on tunable laser diodes for the near infrared, quantum cascade lasers, long-wavelength vertical-cavity laser-diodes and laser diode applications.

He authored or co-authored more than 200 articles (including some 30 invited) on semiconductor optoelectronics in scientific journals and conference proceedings, and co-authored two books. He is a member of the German Informationstechnische Gesellschaft (ITG), and a senior member of the IEEE Lasers and Electro-Optics Society.

Sebastian Wieczorek received his M.S. degree in Theoretical Physics from Adam Mickiewicz University in Poznan, Poland, in 1998, and the PhD. degree in Mathematical Physics from the Free University Amsterdam, The Netherlands, in 2002. For his PhD work he received 2002 IEEE LEOS Graduate Student Award. Currently, he is a faculty member in the Mathematics Research Institute at University of Exeter, UK. His research interests are in the area of applied bifurcation theory and nonlinear dynamics of (semiconductor) laser systems such as excitation-modulated lasers, coupled lasers, lasers with optical injection, lasers with external optical feedback, lasers without population inversion, and photonic crystal lasers.

Weng W. Chow

Distribution

1	MS 0123	LDRD Office, 01011
1	MS1086	Weng Chow, 01123
1	MS0982	Geoffrey Torrington, 05735
1	MS0980	Stephen Gentry, 05703
1	MS0980	Toby Townsend, 05703
1	MS0972	Clinton A. Boye, 05710
1	MS1086	Dan Barton, 01123
1	MS1415	Charles Barbour, 01120
1	MS1421	Jerry Simmons, 01130
1	MS1427	Julia Phillips, 01100

1 Sebastian Wieczorek
Applied Nonlinear Mathematics Department
University of Exeter
Harrison Building, Room 325
North Park Road
Exeter EX4 4QF
UK

2	MS9018	Central Technical Files, 8944
2	MS0899	Technical Library, 4536